Evaluating k–ϵ with One–Equation Turbulence Model

M. M. Rahman[1], A. Meriläinen[1], A. K. M. Sadrul Islam[2] and M. J. Lampinen[1]

[1]Aalto University School of Engineering, Department of Energy Technology
Laboratory of Applied Thermodynamics
P.O. Box 14400, FI–00076 AALTO, Finland
[2]Department of Mechanical & Chemical Engineering,
Islamic University of Technology, Board Bazar,
Gazipur 1704, Bangladesh
[1]E-mail: Mizanur.Rahman@aalto.fi

Abstract

An extended version of the isotropic one–equation model is proposed to account for the distinct effects of low-Reynolds number (LRN) and wall proximity. The turbulent kinetic energy k and the dissipation rate ϵ are evaluated using the R $(= k^2/\tilde{\epsilon})$ transport equation together with some empirical relations. The eddy viscosity formulation maintains the positivity of normal Reynolds stresses and the Schwarz' inequality for turbulent shear stresses. The model coefficients/functions preserve the anisotropic characteristics of turbulence in the sense that they are sensitized to rotational and nonequilibrium flows. The model is validated against a well-documented flow case, yielding predictions in good agreement with the direct numerical simulation (DNS) data. Comparisons indicate that the present model offers some improvement over the Spalart–Allmaras one–equation model.

Keywords: One–equation model, turbulence anisotropy, realizability, nonequilibrium flow.

1. Introduction

One-equation turbulence model enjoys a wide popularity due to its simplicity of implementation and less demanding computational requirements, compared with the standard two-equation k–ϵ and k–ω models. The algebraic model such as Baldwin–Lomax model [1] is efficient from a numerical point of view but lacks generality for not having transport and diffusion effects. However, one-equation model includes transport effects and can be considered as a good compromise between algebraic and two-equation models.

Considerable research is devoted to improving the accuracy of one-equation models, comprising the equilibrium and non-equilibrium flows [2–8]. The Baldwin–Barth (BB) model [2] derived using the k–ϵ closure is among the first one-equation models to be self-consistent by avoiding the use of algebraic length scales. Nevertheless, in the course of transformation some other major assumptions are made that weaken the link with its parent k–ϵ models. As a result, the BB model performs very differently from the underlying k–ϵ model, even in simple equilibrium flows [4]. To a larger extent, the failure of the BB model lies in the destruction

term. Besides, it is sensitive to the free-stream value of the turbulent Reynolds number and yields unexpected results in predicting the separation in attached flows with mild to strong adverse pressure gradients. In addition, the diffusive term that is not directly connected to the k–ϵ model renders the model ill-conditioned near the edge of the shear layers. However, the BB model has good near-wall benign properties like the linear behavior of its transport property, which in turn does not require a finer grid than an algebraic model does [5]. Spalart and Allmaras (SA) [3] derive their model using empirical criteria and arguments from dimensional analysis, having no link to the k–ϵ equations. The motivation for this approach is that the BB model is constrained by assumptions inherited from the k–ϵ model. Note that the SA model is a modified version of the BB model.

Using the Bradshaw–relation [8] (i.e., the shear stress in the boundary layer is proportional to the turbulent kinetic energy), Menter [4], in his transformation from the k–ϵ closure to the one-equation model shows a closer connection than the BB model. Menter also mentions that using the Bradshaw–relation seems to be more effective in nonequilibrium flows. However, transforming the k–ϵ closure may carry many of its deficiencies, such as the bad performance in wall-bounded flows in the presence of mild adverse pressure gradients. It should be emphasized that Menter aims at establishing a firm bond between the one- and two-equation models rather than endorsing a new model for general use. Further modifications to one-equation models based on Menter's transformation of the k–ϵ and k–ω closures are proposed by Elkhoury [5] that have no effect for zero pressure gradient flows. However, they improve the predictive capabilities of the models in wall-bounded nonequilibrium flows compared with the SA model and retain their wall-distance-free feature. Fares and Schröder [6] devise a one-equation model using the findings of the SA and k–ω models that predicts a wide range of flows especially jets and vortical flows more accurately than the SA model while retaining the same quality of results for near-wall flows, and to be more efficient than the k–ω model. Nagano et al. [7] propose a low-Reynolds number (LRN) one-equation model derived from an LRN two-equation k–ϵ model using the modified Bradshaw–relation that accounts for near-wall turbulence. The model provides good results for simple flows and the flow with separation and reattachment.

In the present study, an LRN extension of the BB one-equation turbulence model is proposed and evaluated. This version has several desirable attributes relative to the original BB model: (a) It revives the link between the BB and k–ϵ models via the source/sink and diffusion terms, using the turbulence structure parameter $a_1 = |-\overline{uv}|/k$ (Bradshaw–relation); (b) an eddy damping function f_μ, the length scale of which is explicitly influenced by the mean flow and turbulent variables, is devised to suppress the excessive eddy viscosity in near-wall regions; (c) a physically appropriate time scale is used that never falls below the Kolmogorov (dissipative eddy) time scale; (d) the turbulent Prandtl number σ is adjusted such as to provide substantial turbulent diffusion in the near-wall region; (e) source/sink term coefficients $C_{1,2}$ and C_μ, that depend nonlinearly on both the rotational and irrotational strains are proposed based on the realizability constraints and appropriate experiments. Consequently, the model extends the ability of the BB model to account for nonequilibrium and anisotropic effects, a feature that is missing in the single equation models developed so far.

The performance of the new model is demonstrated through the comparison with the DNS data such as fully developed channel flows. The test case is selected such as to justify the ability of the model to replicate the combined effects of LRN, near-wall turbulence. Since the SA model is not transformed from the k–ϵ closure, it would be interesting to compare the present model predictions with those of the SA model.

2. Turbulence modeling

The principal assumption in deriving the one-equation model is that the turbulent shear stress ($-\overline{uv}$) is proportional to the turbulent kinetic energy (k), which is equivalent to the assumption of Production (P) = Dissipation (ϵ) in standard two-equation k–ϵ models. The second assumption is that $\sigma = \sigma_k = \sigma_\epsilon$. A more detailed derivation can be found in Menter [4]. In collaboration with the Reynolds-averaged Navier-Stokes (RANS) equations, the proposed model determines R by the following transport relation. $R = k^2/\tilde{\epsilon}$ can be enumerated as an undamped tentative eddy viscosity, where the reduced dissipation rate $\tilde{\epsilon} \to 0$ as the wall is approached, while ϵ remains finite. The one-equation turbulence model for high-Reynolds number wall-bounded flows developed by Baldwin and Barth [2] is modified to evaluate R as:

$$\frac{\partial \rho R}{\partial t} + \frac{\partial \rho u_j R}{\partial x_j} = \frac{\partial}{\partial x_j}\left[\left(\mu + \frac{\mu_T}{\sigma}\right)\frac{\partial R}{\partial x_j}\right] + C_1 \rho \sqrt{P\tilde{R}} - C_2 \rho \left(\frac{\partial \tilde{R}}{\partial x_i}\right)^2 \tag{1}$$

subjected to $R_w = 0$ at solid walls. Herein, ρ is the density, μ denotes the molecular viscosity, σ is the appropriate turbulent Prandtl number, the production term $P = -\overline{u_i u_j}(\partial u_i/\partial x_j)$, and the undamped actual eddy viscosity $\tilde{R} = k T_t$, where T_t is the hybrid time scale. Compared with the original Baldwin–Barth (BB) model, the new model replaces R by $\tilde{R}$ from μ_T (eddy-viscosity/diffusion), C_1 (production) and C_2 (destruction) terms that renders the direct coupling between R, k and T_t (i.e., ϵ since T_t contains both k and ϵ), thus reducing the free–stream sensitivity. Equation (1) presents a closure problem with three unknowns and therefore, in order to close it, k and ϵ are evaluated using the R–transport equation together with the Bradshaw [8] and other empirical relations. Alternatively, k and ϵ are represented in terms of R in section 2.5.

`

The Reynolds stresses $\rho \overline{u_i u_j}$ are related to the mean strain rate tensor S_{ij} through the Boussinesq approximation:

$$-\rho \overline{u_i u_j} = 2\,\mu_T\left(S_{ij} - \frac{1}{3}S_{kk}\,\delta_{ij}\right) - \frac{2}{3}\,\rho\,k\,\delta_{ij}, \qquad S_{ij} = \frac{1}{2}\left(\frac{\partial u_i}{\partial x_j} + \frac{\partial u_j}{\partial x_i}\right) \tag{2}$$

The turbulent viscosity is evaluated from

$$\mu_T = C_\mu\,f_\mu\,\rho\,\tilde{R} = C_\mu\,f_\mu\,\rho\,k\,T_t \tag{3}$$

where the eddy viscosity damping function f_μ is obtained by solving the elliptic f_μ equation that envisages LRN and wall proximity effects. However, f_μ relaxes to 1 (one) far from the wall. The model coefficient C_μ is in general a scalar function of the invariants formed on the strain rate S_{ij} and vorticity W_{ij} tensors in question [9]. The vorticity tensor W_{ij} is defined as

$$W_{ij} = \frac{1}{2}\left(\frac{\partial u_i}{\partial x_j} - \frac{\partial u_j}{\partial x_i}\right) \tag{4}$$

The invariants of mean strain rate and vorticity tensors are defined by $S = \sqrt{2 S_{ij} S_{ij}}$ and $W = \sqrt{2 W_{ij} W_{ij}}$, respectively. The detailed functional form of C_μ is determined relying on the constraints such as realizability and appropriate experiments. The formulation of the model coefficients and associated relevant aspects are discussed in some detail in subsequent sections.

2.1. Hybrid time scale T_t

The standard argument to introduce a specific time scale is that near a wall the flow is not turbulent anymore, and hence the use of the dynamic time scale k/ϵ is not appropriate. Employing k/ϵ results in that the time scale vanishes when approaching a wall, where $k \to 0$ and ϵ is non–zero. To avoid this, the Kolmogorov time scale $\sqrt{\nu/\epsilon}$ is used as a lower bound, where the viscous dissipation is dominant. In k–ϵ models, this approach prevents the singularity in the dissipation equation down to the wall. To interpolate smoothly between Kolmogorov and dynamic scales, a hybrid time scale is formed as

$$T_t = \sqrt{\frac{k^2}{\epsilon^2} + C_T^2 \frac{\nu}{\epsilon}} = \frac{k}{\epsilon}\sqrt{1 + \frac{C_T^2}{Re_T}}, \qquad Re_T = \frac{k^2}{\nu\,\epsilon} \tag{5}$$

where ν denotes the kinematic viscosity and Re_T is the turbulence Reynolds number. Equation (5) warrants that the eddy time scale never falls below the Kolmogorov time scale $C_T\sqrt{\nu/\epsilon}$, dominant in the immediate neighborhood of the solid wall. Alternatively, the turbulence time scale is k/ϵ at large Re_T but approaches the Kolmogorov limit $C_T\sqrt{\nu/\epsilon}$ for $Re_T \ll 1$. The empirical constant $C_T = \sqrt{2}$ associated with the Kolmogorov time scale is estimated from the behavior of k in the viscous sublayer [10].

2.2. Coefficient C_μ

The new model appears with recourse to the realizability constraints, reflecting physically necessary conditions for developing a compatible turbulence model. The realizability conditions represent the minimal requirement to prevent a turbulence model from producing nonphysical results [11]. The commonly used isotropic eddy viscosity model with a constant $C_\mu = 0.09$ becomes unrealizable in the case of a large mean strain rate parameter $T_t S$ (when $T_t S > 3.7$), producing negative normal stresses in question and realizability is violated. To ensure realizability, the model coefficient C_μ cannot be a constant. It must be related with the mean flow deformation rate. Accordingly, a new formulation for C_μ as suggested by Gatski and Speziale [9] is adopted:

$$C_\mu = \frac{\alpha_1}{1 - \frac{2}{3}\eta^2 + 2\xi^2}, \quad \eta = \alpha_2 T_t S, \quad \xi = \alpha_3 T_t W \tag{6}$$

The coefficients α_1–α_3 associated with Eq. (6) are given by

$$\begin{aligned}
\alpha_1 &= g\left(\frac{1}{4} + \frac{2}{3}\Pi_b^{1/2}\right), & \alpha_2 &= \frac{3}{8\sqrt{2}}\,g \\
\alpha_3 &= \frac{3}{\sqrt{2}}\alpha_2, & g &= \left(1 + 2\frac{P_k}{\epsilon}\right)^{-1}
\end{aligned} \tag{7}$$

Note that the constants associated with g are slightly modified to reproduce the data of DNS and experiments. The invariant of the Reynolds stress Π_b and production to dissipation ratio P_k/ϵ in Eq. (7) are modeled such that they depend nonlinearly on both the rotational and irrotational strains [12]:

$$\Pi_b = C_\nu \frac{P_k}{\epsilon}, \qquad \frac{P_k}{\epsilon} = C_\nu \zeta^2 \tag{8}$$

with

$$C_\nu = \frac{1}{2\left(1 + T_t S\sqrt{1 + \Re^2}\right)}, \qquad \zeta = T_t S\,\max(1, \Re) \tag{9}$$
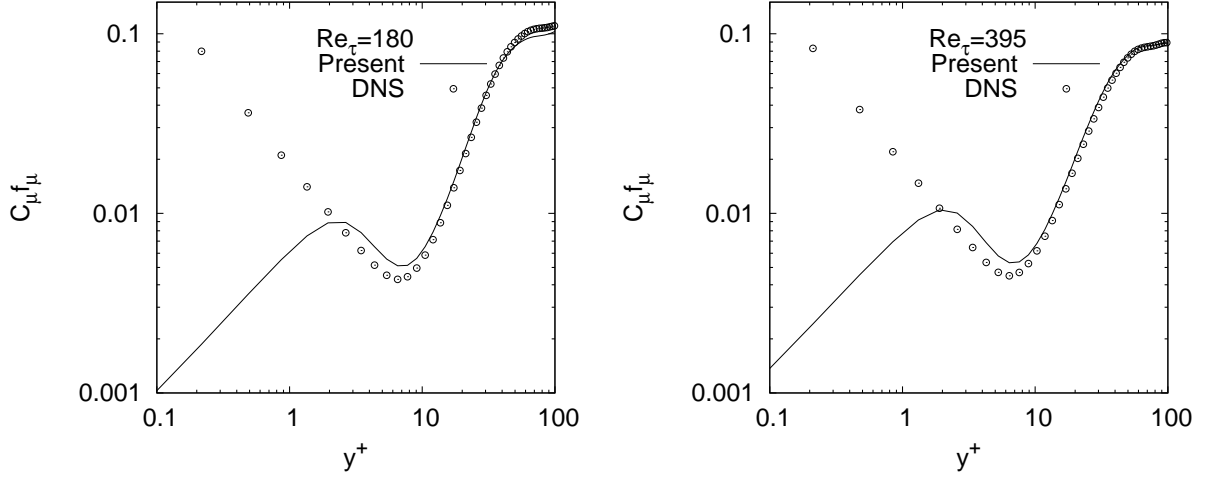
Figure 1: Variations of eddy viscosity coefficient with wall distance in channel flow.

where $\Re = |W/S|$ is a dimensionless parameter that is very useful to characterize the flow. For instance, for a pure shear flow $\Re = 1$, whereas for a plane strain flow $\Re = 0$. It is appropriate to emphasize herein that the calibrated relations for Π_b and P/ϵ can assist the coefficients $(\alpha_1-\alpha_3)$ in responding to both the shear and vorticity dominated flows that are far from equilibrium. Detailed analysis of the model realizability is available elsewhere [12].

2.3. Damping function

The eddy viscosity damping function f_μ faces the distinct effects of LRN and wall proximity in near-wall regions. Alternatively, the primary objective of introducing f_μ to turbulence models is to represent the kinematic blocking by the wall, and is devised pragmatically as

$$f_\mu = 1 - exp\left(-\frac{y}{L}\right), \qquad L^2 = 2\zeta\,(6 + C_\mu Re_T)\sqrt{\frac{\nu^3}{\epsilon}} \qquad (10)$$

where $(\nu^3/\epsilon)^{1/4}$ signifies the Kolmogorov length scale. A plot of $C_\mu f_\mu$ against the DNS data for fully developed turbulent channel flows is shown in Fig. 1 and good correlation is obtained for $y^+ > 1$. For $y^+ \leq 1.5$, $C_\mu f_\mu$ seems likely to increase proportionally to y (i.e., like a single f_μ) in the very near-wall region as evinced by Fig. 1 in comparison with the DNS data [13]. Overall, the adopted form of $C_\mu f_\mu$ converges to replicate the influences of LRN and wall proximity. The product $C_\mu f_\mu \approx 0.09$ (the standard choice for $C_\mu = 0.09$, pertaining to the linear k-ϵ model) remote from the wall to ensure that the model is compatible with the high-Reynolds number turbulence model.

2.4. Other model coefficients

The model coefficients C_1 and C_2 are related to the k-ϵ constants by [2]

$$C_1 = C_{\epsilon 2} - C_{\epsilon 1} = 0.48, \qquad C_2 = (C_{\epsilon 2} - C_{\epsilon 1})\frac{C_\mu^*\sqrt{C_\mu^*}}{\kappa^2} \approx 0.08 \qquad (11)$$

where $\kappa = 0.41$ is the von Karman constant. The coefficients C_1 and C_2 are calculated based on the values of the standard k-ϵ closure where $C_{\epsilon 1} = 1.44$, $C_{\epsilon 2} = 1.92$ and $C_\mu^* = 0.09$.
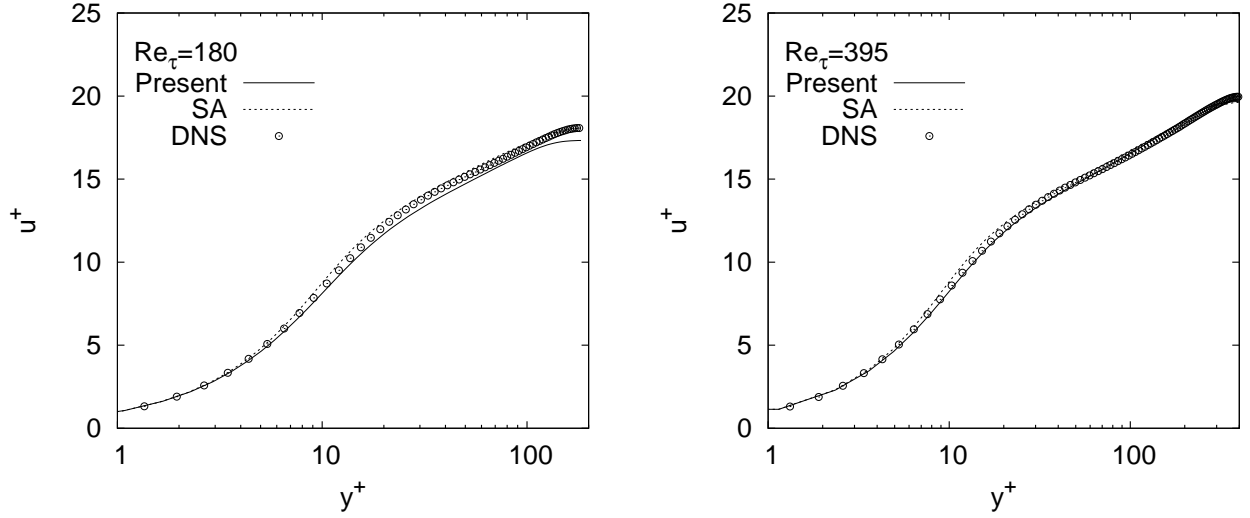
Figure 2: Mean velocity profiles of channel flow.

However, the necessity to account for changes in C_1 and C_2 is desirable in order to include the local anisotropy of turbulence as is practised in the k-ϵ turbulence model [12]. To explore the anisotropic situation, C_1 and C_2 are devised as a function of mean shear and vorticity parameters (i.e., $T_t S$ and $T_t W$, respectively):

$$C_1 = 2\sqrt{\Pi_b^*}\left(1 - \sqrt{\Pi_b^*}\right), \qquad C_2 = 2\left(C_\mu - \frac{\left|\tilde{C}_\mu\right| - \tilde{C}_\mu}{C_T^2}\right) \tag{12}$$

where $\tilde{C}_\mu = C_\mu^* - C_\mu$, $C_\mu^* = 0.09$ and $\sqrt{\Pi_b^*} = C_\mu \zeta$ is essentially identical to Eq. (9), however, with the exception that C_ν is replaced by C_μ. It can be stressed that the shear/vorticity parameter certainly induces compatible changes in $C_{1,2}$ which account for the anisotropy of turbulence. Remarkably, $C_1 \approx 0.42$ and $C_2 \approx 0.18$ in the log layer of a channel flow with $\zeta(\Re = 1) \approx 3.3$. However, at some value of $C_\mu = C_\mu(T_t S, T_t W)$, C_2 will reach 0.08 as given in Eq. (11). In principle, the reconstruction of $C_{1,2}$ assists qualitatively in predicting turbulent flows with separation and reattachment as shown in the computation section.

The budgets of k and ϵ from the DNS data suggest that the role of turbulent diffusion in the near-wall region is substantial. Accordingly, the Prandtl number σ is modeled, rather than being assigned constant value (unlike the commonly adopted practice with $\sigma \approx 1$):

$$\sigma = C_\mu + f_\mu/C_T \tag{13}$$

The model coefficients σ is developed so that sufficient diffusion is obtained in the vicinity of the wall. This contrivance tends to successfully predict the kinetic energy and dissipation rate profiles from the R–transport equation. Nevertheless, $C_\mu \approx 0.3$ and $f_\mu = 1.0$ in the free-stream region and therefore, $\sigma \approx 1$ is recovered therein.

2.5. Evaluation of k and ϵ

The professed interest herein is to represent k and ϵ in term of R in order to evaluate $\tilde{R}$ (and therefore μ_T) in Eq. (3). Probably, it is the most essential step, since the generality of the reconstructed k and ϵ must be guaranteed through a wide range of flows. The most appropriate
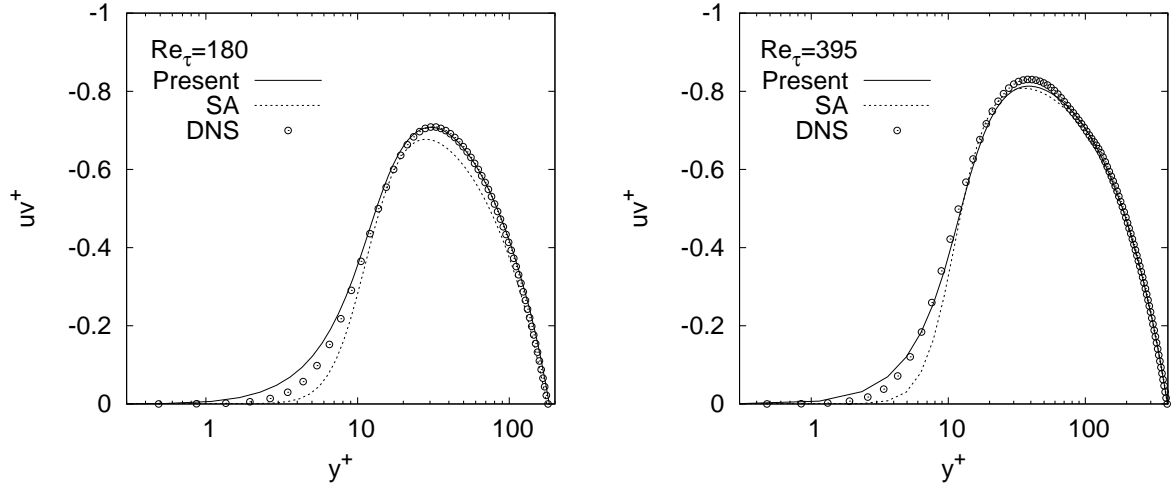
Figure 3: Shear stress profiles of channel flow.

assumption concerning such a reconstruction is the Bradshaw hypothesis [8] implemented directly into many turbulence models [6]. With the Bradshaw–relation, k may be expressed using the tentative eddy viscosity $(C_\mu f_\mu^n R)$ through the turbulence structure parameter:

$$\frac{|-\overline{uv}|}{k} = a_1 = C_\mu f_\mu^n R \frac{S}{k} \tag{14}$$

where the turbulence structure parameter $a_1 = \sqrt{C_\mu}$. The exponent n of f_μ is chosen to be $n = 0.8$ to fit DNS/experimental data and sensibly, without the loss of generality. To avoid the implicit formulation, Eq. (3) is not used to form Eq. (14) and the purpose herein is to revive the link between the BB and k–ϵ models via the source/sink and diffusion terms utilizing a_1.

Recent DNS and experimental data indicate that the Bradshaw–hypothesis is neither exactly valid in the viscous sublayer of the turbulent boundary layer nor in the free shear layers [6, 7]. However, it is to be expected that the introduction of Eq. (14) with the one–equation model will actually lead to improved predictions of nonequilibrium flows [4]. Therefore, k can be determined from Eq. (14) as

$$k = \sqrt{C_\mu} R\, S\, f_\mu^{0.8} \tag{15}$$

Since $S \rightarrow 0$ away from the wall (i.e., free-stream region), k given by Eq. (15) is insufficient there. In fact, the region where S is locally zero is bridged mutually by the diffusion and convection terms in the k-ϵ turbulence model. With the assistance of [7], the mean strain rate correction S_α away from the wall is determined by numerical optimization:

$$S_\alpha = \frac{2C_\alpha f_\alpha}{3\nu} \left(\frac{\sqrt{u_i^2/2}}{1 + \mu_T/\mu} \right)^2 \tag{16}$$

with

$$C_\alpha = \sqrt{C_\mu^2 + \frac{\nu}{\nu + R}}, \qquad f_\alpha = 1 - exp\left(-\frac{\mu_T}{36\mu} \right) \tag{17}$$

where $u_i = \sqrt{u^2 + v^2 + w^2}$ is the velocity magnitude and (u,v,w) is the velocity vector in Cartesian coordinates. The expression C_α uses $(\nu + R)$ to avoid the singularity in the near–wall region since $R \to 0$ there.

Note that C_μ depends nonlinearly on both the shear and vorticity parameters and therefore, the structure parameter $a_1 = \sqrt{C_\mu}$ used in reconstructing k is no longer constant. However, the Bradshaw–relation Eq. (14) has no meaning for flows without shear. To extend the predictive capability, a modification is proposed to account for the effect of mean rotation rate on the mean strain rate:

$$\tilde{S} = S - \frac{|\eta_1| - \eta_1}{C_T}, \qquad \eta_1 = S - W \tag{18}$$

The advantage of this formulation is that k (and therefore, the turbulence eddy viscosity) is reduced in the regions where the magnitude of the vorticity exceeds that of the strain rate, such as in the vortex core. Nevertheless, the overwhelming majority of applications of turbulence models is for shear dominated flows, where the one–equation model is probably well suited. Thus, Eq. (15) can be reconstructed as follows:

$$k = f_\mu^{0.8} \sqrt{C_\mu} R \, S_k, \qquad S_k = \sqrt{\tilde{S}^2 + S_\alpha^2} \tag{19}$$

The value of ϵ plays an important role in evaluating the hybrid time scale T_t accompanied by the turbulence eddy viscosity μ_T, and is reconstructed as follows:

$$\epsilon = \sqrt{\epsilon_w^2 + \tilde{\epsilon}^2}, \qquad \tilde{\epsilon} = \frac{k^2}{\nu + R} \tag{20}$$

where ϵ_w signifies the wall-dissipation rate that equals to the viscous-diffusion rate [14] and is modeled as

$$\epsilon_w = 2 A_\epsilon \nu \left(\frac{\partial u}{\partial y} \right)_w^2 \approx 2 A_\epsilon \nu \tilde{S}^2 \tag{21}$$

where A_ϵ is a function of the Reynolds number. Experimental and DNS data of flat plate and channel flows indicate that $0.05 < A_\epsilon < 0.11$, with a preference for higher values at larger Reynolds numbers [13]. In the current work, $A_\epsilon = C_\mu^* = 0.09$ is adopted. Apparently, the contribution of ϵ_w to ϵ is confined within the wall layer.

3. Computations

To validate the generality and efficacy of the proposed model, fully developed channel flows are considered. To evaluate the model reliability and accuracy, the present model predictions are compared with those from the SA model [3]. However, compared with the SA model, the new model is additionally sensitized to nonequilibrium and anisotropic effects (i.e., anisotropic model coefficients, depending nonlinearly on both the rotational and irrotational strains). A cell centered finite-volume scheme combined with an artificial compressibility approach is employed to solve the flow equations [15, 16].

The computation is carried out for fully developed turbulent channel flows at $Re_\tau = 180$ and 395 for which turbulence quantities are available from the DNS data [13] . The calculation is conducted in the half-width of the channel, using one–dimensional RANS solver. The computation involving a 1×64 nonuniform grid refinement is considered based on the grid
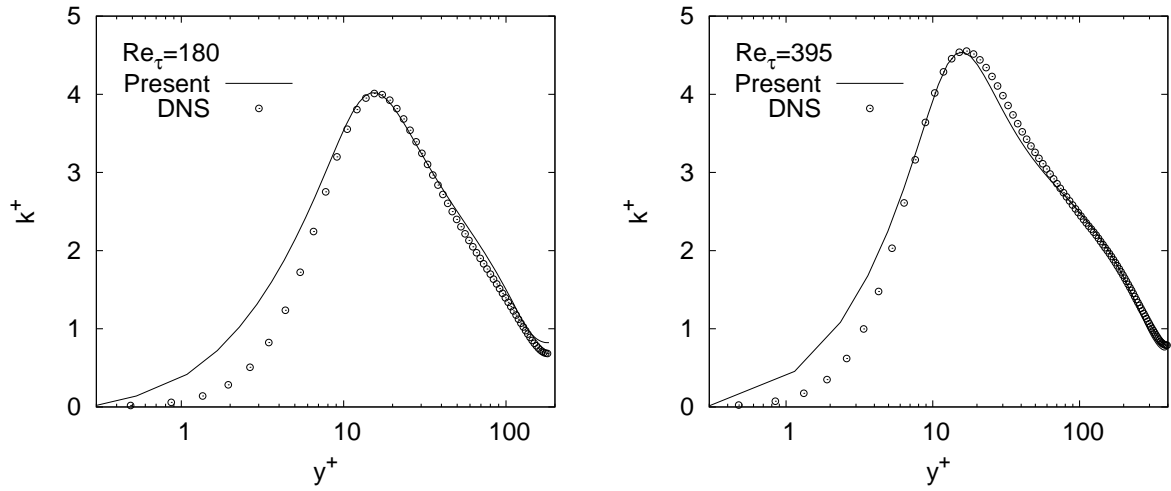
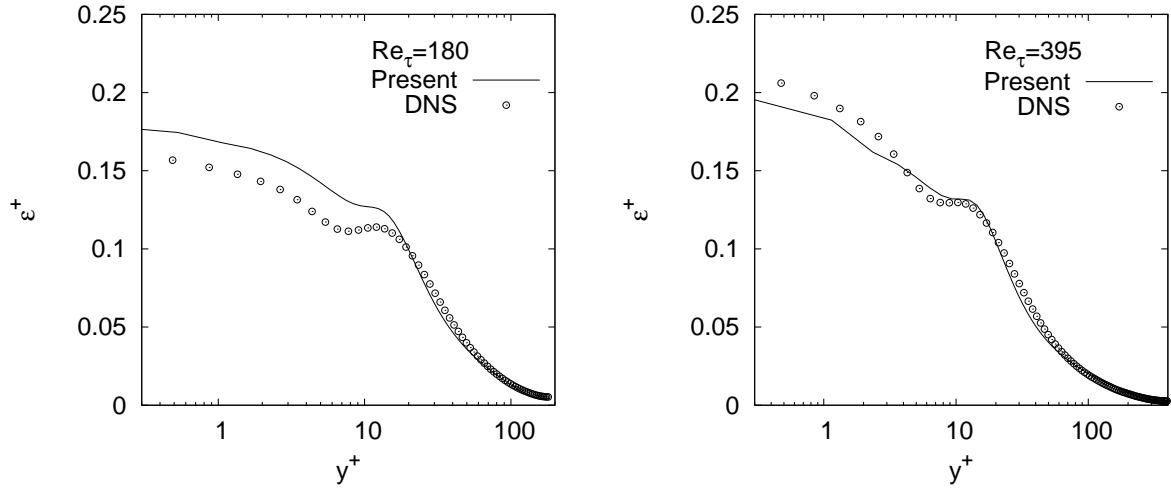Figure 4: Turbulence kinetic energy profiles of channel flow.

Figure 5: Dissipation rate profiles of channel flow.

independence test. To ensure the resolution of the viscous sublayer the first grid node near the wall is placed at $y^+ \approx 0.3$. Comparisons are made by plotting the results in the form of $u^+ = u/u_\tau$, $k^+ = k^+/u_\tau^2$, $\overline{uv}^+ = \overline{uv}/u_\tau^2$ and $\epsilon^+ = \nu\epsilon/u_\tau^4$ versus y^+.

Figure 2 shows the velocity profiles for different models. Predictions of the present and SA models agree well with the DNS data. However, at $Re_\tau = 180$ the relative errors on the prediction of Re_τ are evaluated as $+2\%$ (averaged value) and -1.7% for the present and SA models, respectively. Profiles of turbulent shear stresses are displayed in Figure 3. Agreement of all model predictions with the DNS data is fairly good. It seems likely that the present model returns superior predictions in near-wall regions relative to the SA model.

Further examination of the model performance is directed to the k^+ profiles as portrayed in Fig. 4. As is evident, k^+ is somewhat overpredicted in the near-wall region. This is probably due to the improper behavior of the Bradshaw–relation employed to evaluate k. Figure 5 exhibits the profiles of ϵ^+ from the present computations that provides a maximum ϵ^+ at the wall which is more in line with the experimental and DNS data. Nevertheless, ϵ^+ is over-
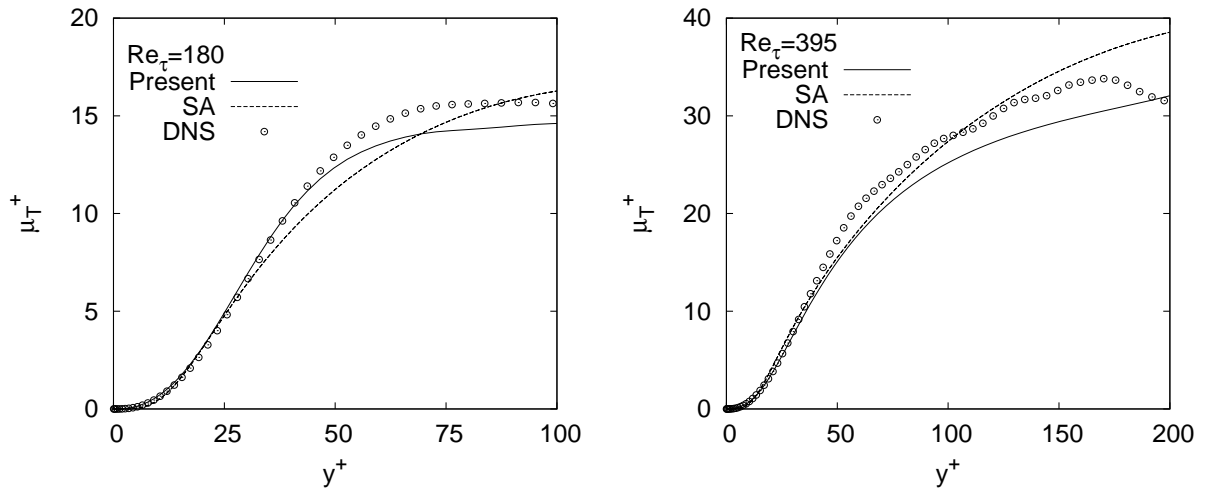
Figure 6: Turbulent eddy viscosity profiles of channel flow.

predicted/underpredicted in near-wall regions. The observed discrepancy might be due to the limitation of the proposed near-wall correction ϵ_w in Eq. (21). Figure 6 shows the turbulent eddy viscosity profiles. As notable from the figure, both the SA and present models reproduce the correct near-wall behavior, comparable with the DNS data. However, both model predictions are inaccurate beyond $y^+ = 50$. Surprisingly, this inaccuracy has little impact on the mean flow and other turbulent parameters since they are reasonably predicted.

4. Conclusions

The present study reconstructs the Baldwin–Barth model to be more consistent with the k–ϵ models. Contrasting the predicted results with DNS data demonstrates that the new model returns predictions comparable with the SA model. Compared with the SA model, the new model is additionally sensitized to nonequilibrium and anisotropic effects. In particular, the present model may be a good choice for engineering applications, since it can easily be extended to a nonlinear eddy viscosity model.

References

1. Baldwin BS, Lomax H: Thin layer approximation and algebraic model for separated turbulent flows. *AIAA Paper*, 78-257 (1978).
2. Baldwin BS, Barth TJ: A one-equation turbulence transport model for high-Reynolds number wall-bounded flows. *NASA TM-102847* (1990).
3. Spalart PR, Allmaras SR: A one-equation turbulence model for aerodynamic flows. *AIAA Paper No. 92-0439* (1992).
4. Menter FR: Eddy viscosity transport equations and their relation to the k–ϵ model. *ASME J. Fluids Engng.*,119, 876-884 (1997).
5. Elkhoury M: Assessment and modification of one-equation models of turbulence for wall-bounded flows. *ASME J. Fluids Engng.* 129, 921-928 (2007).
6. Fares E, Schröder W: A general one-equation turbulence model for free shear and wall-bounded flows. *Flow, turbulence and combustion* 73, 187-215 (2004).
7. Nagano Y, Pei CQ, Hattori H: A new low-Reynolds-number one-equation model of turbulence. *Flow, turbulence and combustion* 63, 135-151 (1999).

8. Bradshaw P, Ferriss DH, Atwell NP: Calculation of boundary layer development using the turbulent energy equations. *J. Fluid Mech.* 23, 31-64 (1967).

9. Gatski TB, Speziale CG: On the explicit algebraic stress models for complex turbulent flows. *J. Fluid Mech.* 254, 59-78 (1993).

10. Rahman MM, Siikonen T: Modifications for an explicit algebraic stress model, *Int. J. Numer. Meth. Fluids* 35(2), 221-245 (2001).

11. Lumley JL: Computational modeling of turbulent flows. *Advances in Appl. Mech.* 18, 124-176 (1978).

12. Rahman MM, Siikonen T: An eddy viscosity model with elliptic relaxation approach. *Int. J. Heat Fluid Flow* 30, 319-330 (2009).

13. Mansour NN, Kim J, Moin P: Reynolds-stress and dissipation-rate budgets in a turbulent channel flow. *J. Fluid Mech.* 194, 15-44 (1988).

14. Patel VC, Rodi W, Scheuerer G: Turbulence models for near-wall and low Reynolds number Flow: A review. *AIAA J.* 23(9), 1308-1319 (1985).

15. Rahman MM, Siikonen T: An artificial compressibility method for incompressible flows. *Numer. Heat Transfer, Part B* 40, 391-409 (2001).

16. Rahman MM, Siikonen T: An artificial compressibility method for viscous incompressible and low Mach number flows. *Int. J. Numer. Meth. Engng.* 75, 1320-1340 (2008).

5th BSME International Conference on Thermal Engineering

Effects of Curvature on Unsteady Solutions through a Curved Square Duct Flow

Md. Saidul Islam[a]* and Rabindra Nath Mondal[b]

[a] Mathematics Discipline; Science, Engineering and Technology School, Khulna University, Khulna-9208, Bangladesh
[b] Department. of Mathematics, Faculty of Science, Jagannath University, Dhaka-1100, Bangladesh
Email: rnmondal71@yahoo.com

Abstract

   The present study addresses numerical prediction of fully developed two-dimensional laminar flow of viscous incompressible fluid through a curved square duct with curvature ranging from 0.001 to 0.5. Numerical calculations are carried out over a wide range of the Dean number $0 < Dn \leq 6000$ with a temperature difference between the vertical sidewalls for the Grashof number Gr = 1000, where the outer wall is heated and the inner wall cooled. Spectral method is used as a basic tool to solve the system of non-linear differential equations. First, we investigated steady solutions by using Newton-Raphson iterations method. As a result, a complex structure of steady solutions with two- and multi-vortex solutions is obtained. Then, in order to investigate the non-linear behavior of the unsteady solutions, time evaluations calculations are performed and the transition between two types of solutions is determined by drawing the phase spaces of the time evolution solutions. It is found that the unsteady flow undergoes in the scenario '*steady-state $\rightarrow$ periodic $\rightarrow$ multi-periodic $\rightarrow$ chaotic*', if the Dean number is increased no matter what the curvature is. Secondary flow patterns, axial flow distribution and temperature profiles on the flow characteristics are also obtained.

Nomenclature			
Dn	: Dean number	T	: Temperature
g	: Gravitational acceleration	u	: Velocity components in the $x-$direction
Gr	: Grashof number	v	: Velocity components in the $y-$direction
h	: Half height of the cross section	w	: Velocity components in the $z-$direction
d	: Half width of the cross section	x	: Horizontal axis
L	: Radius of the curvature	y	: Vertical axis
P_r	: Prandtl number	z	: Axis in the direction of the main flow
t	: Time	λ	: Resistance coefficient
Greek letters			
δ	: Curvature of the duct	υ	: Kinematic viscosity
ρ	: Density	κ	: Thermal diffusivity
ψ	: Sectional stream function	μ	: Viscosity

* Corresponding author. Tel.: +88-01710851580; Fax: +88-02-7113752.
E-mail address: rnmondal71@yahoo.com

1. Introduction

The study of flows and heat transfer through curved ducts and channels has been and continues to be an area of paramount interest of many researchers because of the diversity of their practical applications in fluids engineering, such as in fluid transportation, turbo machinery, refrigeration, air conditioning systems, heat exchangers, ventilators, centrifugal pumps, internal combustion engines and blade-to-blade passage for cooling system in modern gas turbines. The flow through curved a duct shows physically interesting features under the action of centrifugal force caused by the curvature of the duct. The presence of curvature produces centrifugal forces which acts at right angle to the main flow direction and creates secondary flows. Dean [1] was the first who formulated the problem in mathematical terms under the fully developed flow conditions and showed the existence of a pair of counter rotating vortices in a curved pipe. The readers are referred to Berger *et al.* [2], Nandakumar and Masliyah [3] and Yanase *et al.* [4] for some outstanding reviews on curved duct flows.

Considering the non-linear nature of the Navier-Stokes equation, the existence of multiple solutions does not come as a surprise. The solution structure of fully developed flow is commonly present in a bifurcation diagram which consists of a number of lines (branches) connecting different possible solutions. These branches can bifurcate and show multiple solutions in limit points (Mondal, [5]). An early complete bifurcation study of two-dimensional flow through a curved duct of square cross section was conducted by Winters [6]. Wang and Yang [7] performed numerical as well as experimental investigations of periodic oscillations for the fully developed flow in a curved square duct. Unsteady flow characteristics through a curved rectangular duct were investigated in detail by Yanase *et al.* [8]. Recently, Mondal *et al.* [9] performed comprehensive numerical study on fully developed bifurcation structure and stability of two-dimensional (2D) flow through a curved duct with square cross section and found a close relationship between the unsteady solutions and the bifurcation diagram of steady solutions. The flow through a curved duct with differentially heated vertical sidewalls has another aspect because secondary flows promote fluid mixing and heat transfer in the fluid. Recently, Mondal *et al.* [10] performed numerical investigations of non-isothermal flows through a curved duct with square cross section, where they studied the flow characteristics with the effects of secondary flows on convective heat transfer.

In the present study, a numerical result is presented for the fully developed two-dimensional flow of viscous incompressible fluid through a curved square duct with various curvatures. Investigating effect of curvature on unsteady solutions is an important objective of the present study.

2. Mathematical Formulations

Consider an incompressible viscous fluid streaming through a curved duct with square cross section whose width or height is $2d$. The coordinate system with the relevant notations is shown in Fig. 1. It is assumed that the outer wall of the duct is heated while the inner one cooled. The temperature of the outer wall is $T_0 + \Delta T$ and that of the inner wall is $T_0 - \Delta T$, where $\Delta T > 0$. The x, y and z axes are taken to be in the horizontal, vertical, and axial directions, respectively. It is assumed that the flow is uniform in the axial direction, and that it is driven by a constant pressure gradient G along the center-line of the duct, i.e. the main flow in the axial direction as shown in Fig. 1. The variables are non-dimensionalized by using the representative length d and the representative velocity $U_0 = v/d$. We introduce the non-dimensional variables defined as

$$u = \frac{u'}{U_0}, \qquad v = \frac{v'}{U_0}, \qquad w = \frac{\sqrt{2\delta}}{U_0}w', \qquad x = \frac{x'}{d}, \qquad \overline{y} = \frac{y'}{d}, \qquad z = \frac{z'}{d}$$

$$T = \frac{T'}{\Delta T}, \quad t = \frac{U_0}{d}t', \quad \delta = \frac{d}{L}, \quad P = \frac{P'}{\rho U_0^2}, G = \frac{\partial P'}{\partial z'}\frac{d}{\rho U_o^2}$$

where u, v, and w are the non-dimensional velocity components in the x, y, and z directions, respectively; t is the non-dimensional time, P the non-dimensional pressure, δ the non-dimensional curvature, and temperature is non-dimensionalized by ΔT. Henceforth, all the variables are nondimensionalized, if not specified.

The sectional stream function ψ is introduced as

$$u = \frac{1}{1+\delta x}\frac{\partial \psi}{\partial \overline{y}}, v = -\frac{1}{1+\delta x}\frac{\partial \psi}{\partial x}. \tag{1}$$

Then the basic equations for w, ψ and T are derived from the Navier-Stokes equations and the energy equation under the *Boussinesq approximation* as,
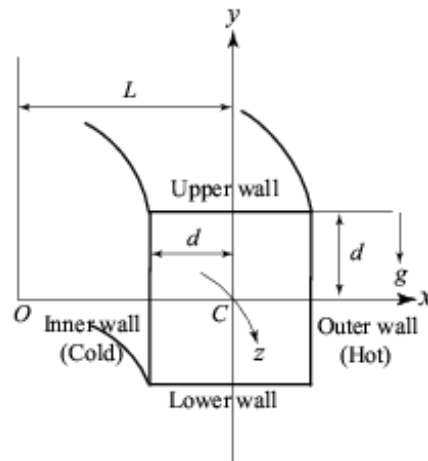
Fig. 1. Coordinate system of the curved duct

$$(1+\delta x)\frac{\partial w}{\partial t}+\frac{\partial(w,\psi)}{\partial(x,y)}-D_n+\frac{\delta^2 w}{1+\delta x}=(1+\delta x)\Delta_2 w-\frac{\delta}{(1+\delta x)}\frac{\partial \psi}{\partial y}w+\delta\frac{\partial w}{\partial x} \tag{2}$$

$$\left(\Delta_2-\frac{\delta}{1+\delta x}\frac{\partial}{\partial x}\right)\frac{\partial \psi}{\partial t}=-\frac{1}{(1+\delta x)}\frac{\partial(\Delta_2\psi,\psi)}{\partial(x,y)}+\frac{\delta}{(1+\delta x)^2}\times\left[\frac{\partial \psi}{\partial y}\left(2\Delta_2\psi-\frac{3\delta}{1+\delta x}\frac{\partial \psi}{\partial x}+\frac{\partial^2\psi}{\partial x^2}\right)-\frac{\partial \psi}{\partial x}\frac{\partial^2\psi}{\partial x\partial y}\right]+\frac{\delta}{(1+\delta x)^2}$$

$$\times\left[3\delta\frac{\delta^2\psi}{\partial x^2}-\frac{3\delta^2}{1+\delta x}\frac{\partial \psi}{\partial x}\right]-\frac{2\delta}{1+\delta x}\frac{\partial}{\partial x}\Delta_2\psi+w\frac{\partial w}{\partial y}\times\Delta_2^2\psi-Gr(1+\delta x)\frac{\partial T}{\partial x}, \tag{3}$$

$$\frac{\partial T}{\partial t}+\frac{1}{(1+\delta x)}\frac{\partial(T,\psi)}{\partial(x,y)}=\frac{1}{\Pr}\left(\Delta_2 T+\frac{\delta}{1+\delta x}\frac{\partial T}{\partial x}\right). \tag{4}$$

where

$$\Delta_2\equiv\frac{\partial^2}{\partial x^2}+\frac{\partial^2}{\partial y^2},\quad \frac{\partial(f,g)}{\partial(x,y)}\equiv\frac{\partial f}{\partial x}\frac{\partial g}{\partial y}-\frac{\partial f}{\partial y}\frac{\partial g}{\partial x}. \tag{5}$$

The Dean number D_n, the Grashof number G_r, and the Prandtl number P_r, which appear in Eqs. (2) to (4) are defined as

$$D_n=\frac{Gd^3}{\mu v}\sqrt{\frac{2d}{L}},\quad G_r=\frac{\beta g\Delta Td^3}{v^2},\quad P_r=\frac{v}{k} \tag{6}$$

where μ, v, k and g are the viscosity, the coefficient of thermal expansion, the coefficient of thermal diffusivity and the gravitational acceleration respectively.

The rigid boundary conditions for w and ψ are used as

$$w(\pm1,y)=w(x,\pm1)=\psi(\pm1,y)=\psi(x,\pm1)=\frac{\partial \psi}{\partial x}(\pm1,y)=\frac{\partial \psi}{\partial y}(x,\pm1)=0 \tag{7}$$

and the temperature T is assumed to be constant on the walls as

$$T(1,y)=1,\ T(-1,y)=-1,\ T(x,\pm1)=x. \tag{8}$$

The upper and lower walls are adiabatic. In the present study, Dn and δ are varied while Gr and Pr are fixed as Gr = 1000 and Pr = 7.0 (water).

3. Method of numerical calculation

In order to obtain the numerical solutions, spectral method is used. The main objective of the method is to use the expansion of the polynomial functions that is the variables are expanded in the series of functions consisting of Chebyshev polynomials. The expansion function $\phi_n(x)$ and $\psi_n(x)$ are expressed as

$$\Phi_n(x)=\left(1-x^2\right)C_n(x),\ \Psi_n(x)=\left(1-x^2\right)^2 C_n(x), \tag{9}$$

where $C_n(x) = \cos(n\cos^{-1}(x))$ is the nth order Chebyshev polynomial. $w(x, y, z)$, $\psi(x, y, t)$ and $T(x, y, t)$ are expanded in terms of $\Phi_n(x)$ and $\Psi_n(x)$ as

$$
\left.\begin{array}{l}
w(x, y, z) = \sum\limits_{m=0}^{M} \sum\limits_{n=0}^{N} w_{mn}(t)\Phi_m(x)\Phi_n(y), \\[3mm]
\psi(x, y, t) = \sum\limits_{m=0}^{M} \sum\limits_{n=0}^{N} \psi_{mn}(t)\Psi_m(x)\Psi_n(y), \\[3mm]
T(x, y, t) = \sum\limits_{m=0}^{M} \sum\limits_{n=0}^{N} T_{mn}(t)\Phi_m(x)\Phi_n(y) + x,
\end{array}\right\} \tag{10}
$$

where M and N are the truncation numbers in the x and y directions respectively. The expansion coefficients w_{mn}, ψ_{mn} and T_{mn} are then substituted into the basic Eqs. (2), (3) and (4) and the collocation method is applied. As a result, the nonlinear algebraic equations for w_{mn}, ψ_{mn} and T_{mn} are obtained. The collocation points are taken to be

$$
\left.\begin{array}{ll}
x_i = \cos\left[\pi\left(1 - \dfrac{i}{M+2}\right)\right], & i = 1, ..., M+1, \\[4mm]
y_i = \cos\left[\pi\left(1 - \dfrac{i}{N+2}\right)\right], & j = 1, ..., N+1.
\end{array}\right\} \tag{11}
$$

where $i = 1, ..., M+1$ and $j = 1, ..., N+1$. In the present study, numerical calculations are carried out over a wide range of the Dean number $0 < Dn \le 6000$ and the Grashof number $Gr = 1000$ for the square duct of curvatures ranging from $\delta = 0.001$ to $\delta = 0.5$. For sufficient accuracy of the solutions, we used $M = 20$ and $N = 20$. Steady solutions are obtained by the Newton-Raphson iteration method. Finally, to calculate the unsteady solutions, Crank-Nicolson and Adams-Bashforth methods together with the function expansion and collocation methods are applied to the equations (2) to (4).

4. Resistance coefficient

We use the resistance coefficient λ as one of the representative quantities of the flow state. It is also called the *hydraulic resistance coefficient*, and is generally used in fluids engineering, defined as

$$
\frac{P_1^* - P_2^*}{\Delta z^*} = \frac{\lambda}{dh^*}\frac{1}{2}\rho\left\langle w^*\right\rangle^2, \tag{12}
$$

where quantities with an P_1^* be asterisk denote dimensional ones, $\langle\ \rangle$ stands for the mean over the cross section of the duct and $d_h^* = 4(2d \times 2dl)/(4d + 4dl)$ is the hydraulic diameter. The main axial velocity $\langle w^*\rangle$ is calculated by

$$
\langle\omega^*\rangle = \frac{v}{4\sqrt{2\delta d}}\int\limits_{-1}^{1}dx\int\limits_{-1}^{1}\omega(x, y, t)dy \tag{13}
$$

Here, λ is related to the mean non-dimensional axial velocity $\langle\omega\rangle$ as

$$
\lambda = \frac{4\sqrt{2\delta}Dn}{\langle\omega\rangle^2} \tag{14}
$$

where $\langle w\rangle = \sqrt{2\delta}d / v\langle w^*\rangle$. In this paper, λ is used to find the solution structure of the steady solutions and to find the unsteady solutions by numerical computations.

5. Results and Discussion

5.1 *Steady Solutions*

With the present numerical calculation, we obtain a single but entangled branch of steady solution for $Gr = 1000$ over the Dean number $0 < Dn \le 6000$. To obtain the steady solution, we used path continuation technique as discussed by Mondal [5]. The solution structure of the steady solution is shown in Fig 2(a). An enlargement of Fig. 2(a) is also shown in Fig. 2(b). It is found that the branch starts from point a ($Dn \approx 0$) and goes to the direction of increasing Dn and

decreasing λ up to point b ($Dn = 4823$), where it experiences a smooth turning and goes to the direction of increasing λ and decreasing Dn up to point c ($Dn = 3897$). At point c, the branch experiences another interesting turning and goes to the direction of increasing Dn and decreasing λ up to point d ($Dn = 4976$), where the branch turns very smoothly and goes to the direction of increasing λ and decreasing Dn up to point e ($Dn = 3862$) and then to point f ($Dn = 4156$), and finally extents to increasing Dn through points g and h. It is found that the branch consists of asymmetric two- and four-vortex solutions, which are not shown here for brevity.

(a)   (b)
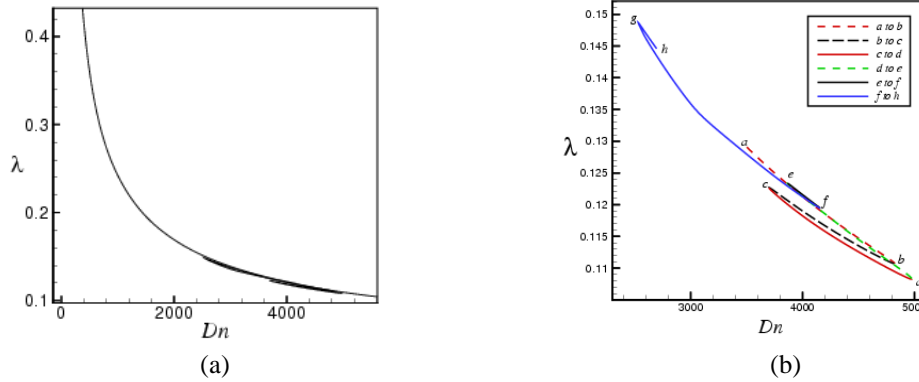
Fig. 2: (a) Solution structure of the steady solution for $Gr = 1000$ and $0 < Dn \le Dn \le 5500$ at $\delta = 0.1$ (b) An enlargement of Fig. 2(a) at $1180 \le Dn \le 5200$.

5.2 *Time evolution of the unsteady solutions*

In order to study the non-linear behavior of the unsteady solutions, we perform time-evolution calculations of λ at various Dn for the curvatures ranging from $\delta = 0.001$ to $\delta = 0.5$ for $Gr = 1000$. However, in this section, we only show the results of unsteady solutions for the curvature $\delta = 0.1$, and complete unsteady solutions ranging from $\delta = 0.001$ to $\delta = 0.5$, are shown in a phase diagram in the next section.
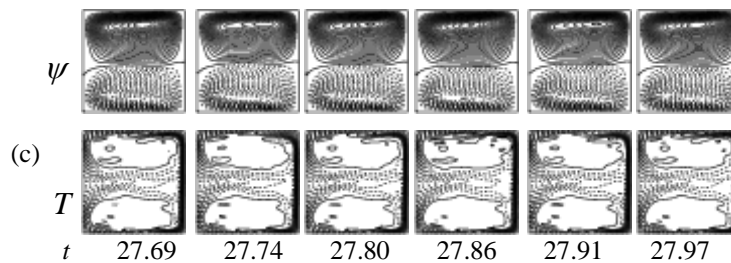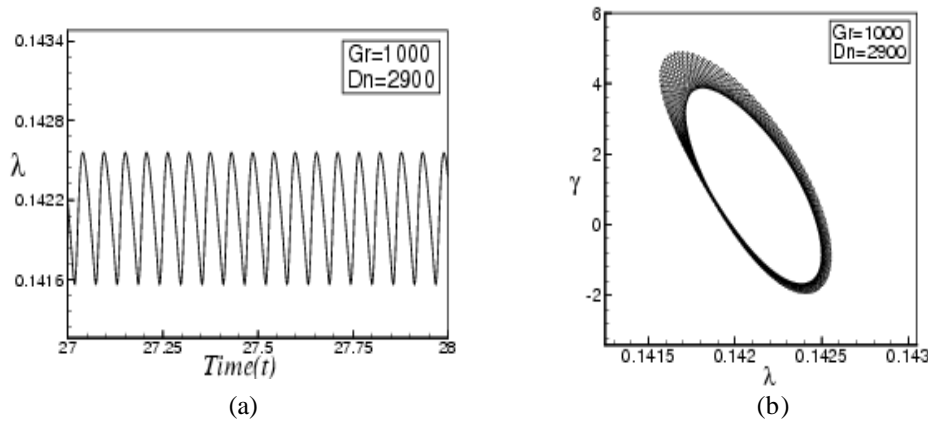

(a)   (b)

Fig. 3: (a) Time evolution of λ for $Dn = 2900$ and $Gr = 1000$ at $\delta = 0.1$ (b) Phase space of the time evolution of λ for $Dn = 2900$ and $Gr = 1000$ (c) Contours of secondary flow patterns (top) and temperature profile (bottom) for one period of oscillation at time $27.69 \le t \le 27.97$.

To investigate the non-linear behavior of unsteady solutions, we studied time evolution of λ for $Dn = 2900$ and $Gr = 1000$ at $\delta = 0.1$ as shown in Fig. 3(a). Figure 3(a) shows that the unsteady flow at $Dn = 2900$ is a periodic solution, which is well justified by drawing a phase spaces as shown in Fig. 3(b). We also show typical contours of secondary flow patterns and temperature profiles, for one period of oscillation at time $27.69 \leq t \leq 27.97$, in Fig. 3(c). It is found that the unsteady solution at $Dn = 2900$ and $Gr = 1000$ at $\delta = 0.1$ is an asymmetric two-vortex solution. Then, we studied the time evolution of λ for $Dn = 2925$ as shown in Fig. 4(a). It is found that the unsteady flow at $Dn = 2925$ is a multi-periodic oscillation. In order to observe the multi-periodic solution more clearly, we draw the phase space as shown in Fig. 4(b). In order to view the change of the flow characteristics as time proceeds, typical contours of secondary flow patterns and temperature profiles are shown in Fig. 4(c). It is found that the unsteady solution at $Dn = 2925$ and $Gr = 1000$ is an asymmetric two-vortex solution. We studied the time evolution of λ for $Dn = 3000$ as shown in Fig. 5(a). It is found that the flow at $Dn = 3000$ is a transitional chaos, which is well justified by drawing the phase space as shown in Fig. 5(b). Then we obtained typical contours of secondary flow patterns and temperature profiles as shown in Fig. 5(c). It is found that the chaotic oscillation at $Dn = 3000$ and $Gr = 1000$ is an asymmetric two-vortex solution.
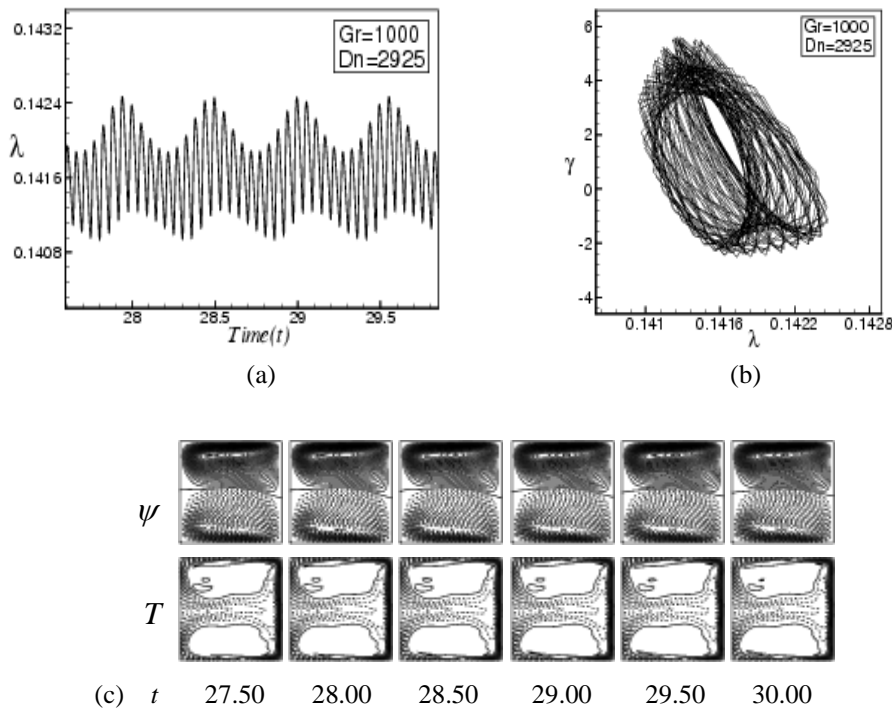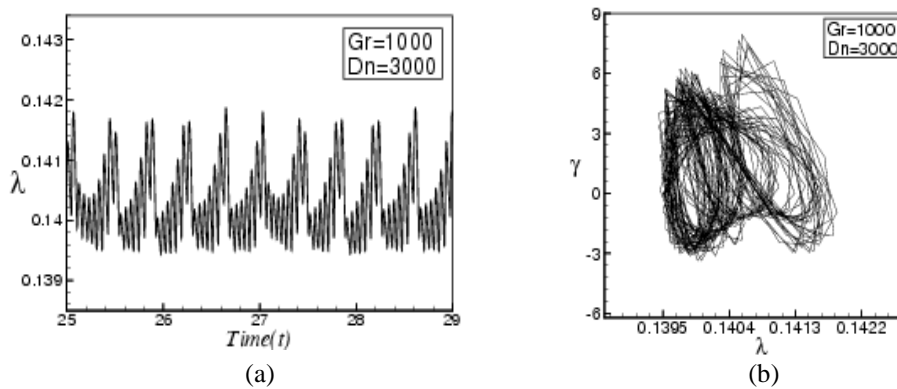

(a)   (b)

(c) t 27.50   28.00   28.50   29.00   29.50   30.00

Fig. 4: (a) Time evolution of λ for $Dn = 2925$ and $Gr = 1000$ at $\delta = 0.1$ (b) Phase space of the time evolution of λ for $Dn = 2925$ (c) Contours of secondary flow patterns (top) and temperature profiles (bottom) for $Dn = 2925$ and $Gr = 1000$ at time $27.50 \leq t \leq 30.00$.
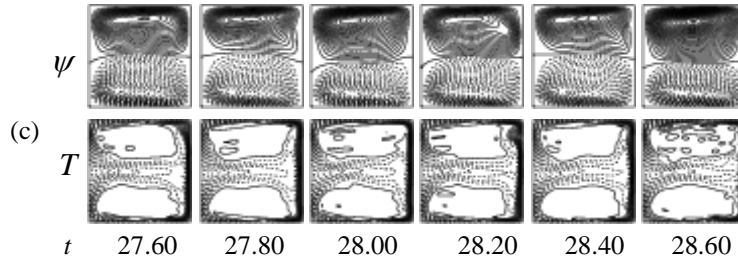

(a)   (b)

| t | 27.60 | 27.80 | 28.00 | 28.20 | 28.40 | 28.60 |

Fig. 5: (a) Time evolution of λ for $Dn = 3000$ and $Gr = 1000$ (b) Phase space of the time evolution of λ for $Dn = 3000$ (c) Contours of secondary flow patterns (top) and temperature profiles (bottom) for $Dn = 3000$ and $Gr = 1000$ at time $27.60 \leq t \leq 28.60$.

It is found that the unsteady solution at $Dn = 3450$ and $Gr = 1000$ is an asymmetric two-vortex solution. We studied the time evolution of λ for $Dn = 3450$ as shown in Fig. 6(a). It is found that the flow at $Dn = 3450$ is a transitional chaos, which is well justified by drawing the phase space as shown in Fig. 6(b). Then we obtained typical contours of secondary flow patterns and temperature profiles as shown in Fig. 6(c). It is found that the chaotic oscillation at $Dn = 3450$ and $Gr = 1000$ is an asymmetric two-vortex solution.
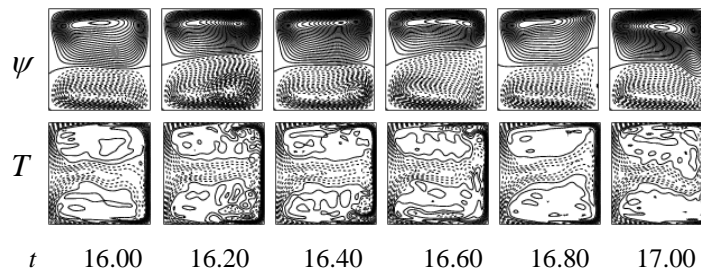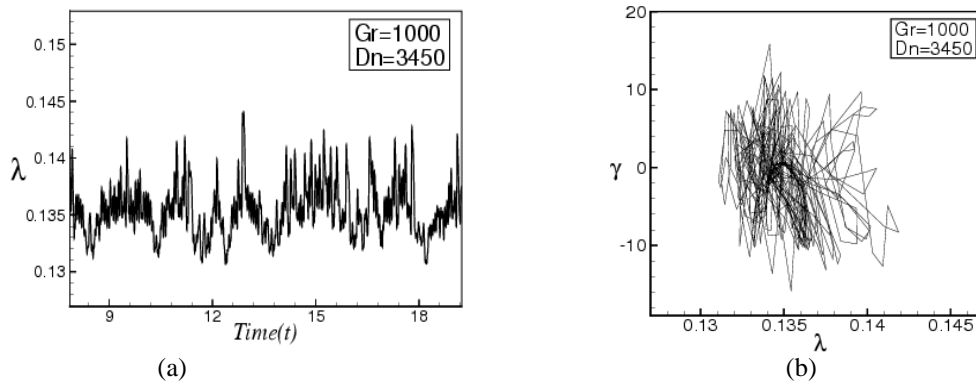

(a)

(b)

| t | 16.00 | 16.20 | 16.40 | 16.60 | 16.80 | 17.00 |

Fig. 6: (a) Time evolution of λ for $Dn = 3450$ and $Gr = 1000$ (b) Phase space of the time evolution of λ for $Dn = 3450$ (c) Contours of secondary flow patterns (top) and temperature profiles (bottom) for $Dn = 3450$ and $Gr = 1000$ at time $16.00 \leq t \leq 17.00$.

5.3 Phase diagram in the $Dn - \delta$ plane

Here, the complete unsteady solutions, obtained by the time evolution computations in the present study, are shown by a phase diagram in Fig. 6 in the $Dn - \delta$ plane for $0 < Dn \leq 6000$ and $0.001 \leq \delta \leq 0.5$ for $Gr = 1000$. In this figure, the circles indicate steady-state solutions, crosses periodic solutions and triangles chaotic solutions. As seen in Fig. 6, the steady-state solution turns into chaotic solution through periodic or multi-periodic oscillation if Dn is increased, no matter what the curvature is.
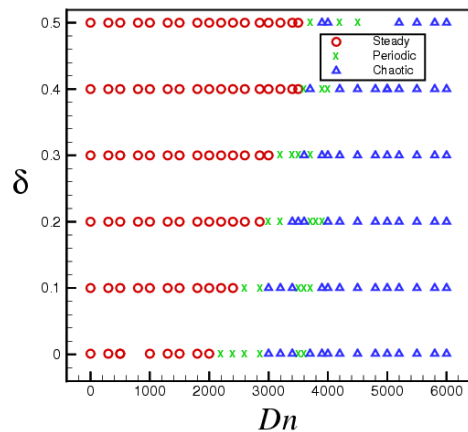
Fig. 6: Distribution of the unsteady solutions in the $Dn - \delta$ plane for $0 < Dn \le 6000$ and curvature $0.001 \le \delta \le 0.5$ for $Gr = 1000$ (O: steady-state solution, ✕: periodic solution and △: chaotic solution).

6. Conclusion

A comprehensive numerical study is presented for the flow characteristics through a curved square duct. Numerical calculations are carried out by using a spectral method and covering a wide range of the Dean numbers $0 < Dn \le 6000$ and the curvature $0.001 \le \delta \le 0.5$ for the Grashof number $Gr = 1000$. First a single branch of asymmetric steady solution is obtained with two- and four-vortex solution. Then, in order to investigate the non-linear behavior of the unsteady solutions, time evaluation calculations as well as their phase space are performed. It is found that the flow becomes steady-state for $Dn < 2900$ but periodic at $Dn = 2900$, multi-periodic solutions for $2925 \le Dn < 3000$ and chaotic solutions for $3000 \le Dn \le 3450$. Thus the unsteady flow undergoes in the scenario "*steady $\rightarrow$ periodic $\rightarrow$ multi-periodic $\rightarrow$ chaotic*", if Dn is increased up to 3450. If the Dean number is increased further, that is, for $Dn > 3450$ the unsteady flow undergoes through various flow instabilities in the scenario "*periodic $\rightarrow$ multi-periodic $\rightarrow$ chaotic $\rightarrow$ periodic $\rightarrow$ chaotic*", if Dn is increased. Secondary flow patterns and temperature profiles are also obtained and it is found that the secondary flow is a two-vortex solution for the unsteady solution.

Acknowledgement

References

[1] Dean, W. R. (1927). Note on the motion of fluid in a curved pipe. *Phil. Mag*. Vol. **4**(20), pp. 208- 223.

[2] Berger, S.A., Talbot, L., Yao, L. S. (1983). Flow in Curved Pipes, *Annual. Rev. Fluid. Mech*., Vol. **35**, pp. 461-512.
[3] Nandakumar, K. and Masliyah, J. H. (1986). Swirling Flow and Heat Transfer in Coiled and Twisted Pipes, *Adv. Transport Process*., Vol. **4**, pp. 49-112.
[4] Yanase, S., Kaga, Y. and Daikai, R. (2002). Laminar flow through a curved rectangular duct over a wide range of the aspect ratio, *Fluid Dynamics Research*, Vol. **31,** pp. 151-183.
[5] Mondal, R. N. (2006). Isothermal and Non-isothermal Flows Through Curved ducts with Square and Rectangular Cross Sections, *Ph.D. Thesis*, Department of Mechanical Engineering, Okayama University, Japan.
[6] Winters, K. H., 1987. A bifurcation study of laminar flow in a curved tube of rectangular cross-section, *J. Fluid Mech.* Vol. **180**, pp. 343--369.
[7] Wang, L. and Yang, T., 2005. Periodic oscillation in curved duct flows, *Physica D*, Vol. **200**, pp. 296—302
[8] Yanase, S, Mondal, R. N. and Kaga, Y. (2005). Numerical study of non-isothermal flow with convective heat transfer in a curved rectangular duct, *International Journal of Thermal Sciences*, Vol. **44** (11), pp. 1047-1060.
[9] Mondal, R. N., Kaga, Y., Hyakutake, T.and Yanase, S. (2007). Bifurcation Diagram for Two- dimensional Steady Flow and Unsteady Solutions in a Curved Square Duct, *Fluid Dynamics Research*. Vol. **39**, pp. 413-446.\
[10] Mondal, R. N., Uddin, M. S. and Yanase, S. (2010). Numerical prediction of non-isothermal flow through a curved square duct, *Int. J. Fluid Mech. Research*, Vol. **37(1)**, pp. 85-99.

5th BSME International Conference on Thermal Engineering

Pulsatile non-Newtonian blood flow through a model of arterial stenosis

Mir Golam Rabby, Abdur Razzak, Md. Mamun Molla*

Dept. of Electrical Engineering & Computer Science, North South University, Dhaka, 1229, Bangladesh,

Abstract

In this research, we numerically investigate the physics of a pulsatile non-Newtonian flow confined within a two-dimensional (2D) axisymmetric pipe with an idealized stenosis using the finite volume method. The governing Navier-Stokes equations have been modified using the Cartesian curvilinear coordinates to handle the complex geometry, such as, arterial stenosis. The flow is characterized by the Reynolds number at 300 which are appropriate for the large arteries. For the non-Newtonian blood flow, the Cross models is used along the Newtonian model. The numerical results are presented in terms of the velocity, pressure distribution, wall shear stress as well as the streamlines indicating the recirculation zones at the post stenotic region.

Nomenclature

f_c	center frequency
Re	Reynolds number
Greek symbols	
μ	viscosity of fluid
ρ	density of fluid
τ_w	wall shear stress
Subscripts	
D	diameter of artery
p	pressure

1. Introduction

In case of pulsatile flow it remains difficult to measure correctly the arterial wall shear stress (WSS) included by a stenosis. According to Ku [1], when WSS is estimated experimentally, errors of 20-50% may occur. Previous studies hardly says that the result of non-Newtonian fluid behavior through the vessel (Bharadvaj *et al.*, [2]; Perktold *et al.*, [3], [4]). On the other hand, the assumption of Newtonian behavior of blood is acceptable for large arteries because of high shear rate flow. When share rate low (0.1 s^{-1}) which is the case of small arteries and the downstream region of the stenosis, the Non-Newtonian behavior of blood flow is acceptable. It has also marked out that some diseased condition like severe myocardial

---

infarction, cerebrovascular diseases and hypertension, blood exhibits remarkable non-Newtonian properties (Chien, [5]).

The existence of a stenosis makes an artery narrowing which makes the recirculating flows through the arteries which are reverse to the healthy artery (Deplano et al. [6]). The interaction between the fluid mechanics variables and atherosclerotic infection reveals a powerful association amidst reduced WSS, oscillating WSS, intimal condensing and plaque formation, while the sites of high WSS are generally freed (Giddens et al., [7]). It has been already proved that vascular fluid dynamics play an important role in the development of arterial stenosis, one of the most widespread diseases in human beings, which is caused due to the deposits of cholesterol in arterial wall. Many studies have been done so far to observe the effect of stenosis when blood flows through the narrowed segment of the artery, considering blood as a Newtonian fluid.

Blood will be treated as non Newtonian incompressible viscoelastic fluid. According to Berger and Jou [8], if the shear rate is greater than 100 s^{-1}, the blood behaves like a Newtonian fluid and it's viscosity approaches as an asymptotic value, μ = 3.45×10^{-3} Pa·s. However, if the shear rate of the blood flow falls down this threshold, its viscosity increases and non-Newtonian fluid behaviors begin to exhibit. The down payments of cholesterol on the arterial wall and expansion of the connective tissues in the wail pattern plaques which grow inward and constraint the body-fluid flow. Stenosis has a convoluted leverage on body-fluid flow through and beyond the tapered segment of artery.

Numerical simulation of arterial stenosis offers a non-invasive entails of getting comprehensive flow patterns associated with the disease. It provision information beyond that accessible from untested study. It can furthermore characterise the specific function performed by the geometry of the partition, the kind and feature of the flow. Fry [9] first postulated that high shear stresses on the arterial wall would injure the vessel wall, and lead to atherogenesis. Atherogenesis originated in the low shear regions (Caro *et al.,* [10]). The blood flow in the human body is pulsatile in nature; the temporal variety of the shave tension might be significant (Ku et al., [11]). And the spatial variety of the wall shear has furthermore been enquired as a likely causative agency by Lie et al. [12].

2. Formulation of The Problem

2.1. The Cross Model for the non-Newtonian Viscosity

Here $\mu = \mu(\dot{\gamma})$ represents the molecular viscosity for non-Newtonian fluid. The value of μ is a function of the norm of the shear rate $\dot{\gamma}$. In a Newtonian model for the blood viscosity, the value of μ is treated as a constant, usually set to $\mu_{\infty} = 3.45 \times 10^{-3}$ Pa·s. However, for non-Newtonian fluid behavior, Cross proposed a shear rate dependent viscosity model (which is often referred to as the Cross model). The Cross model [13] assumes the following functional relation between the molecular viscosity and the shear rate:

$$\mu = \mu_{\infty} + \left(\mu_0 - \mu_{\infty}\right)\left[1 + \left(\frac{|\dot{\gamma}|}{\gamma_c}\right)^m\right]^{-1} \tag{1}$$

Where μ_0 = 0.0364 Pa·s is the usual molecular blood viscosity at very low shear rates, γ_c = 2.63 s^{-1} is the reference shear rate and m = 1.45 is the model constant. Here cross model is using for calculating the molecular viscosity of the non-Newtonian fluid at the resolved scale.

2.2. Test Case and Governing Equation:

The geometry of 2D pipe is a one-sided cosine-shaped stenosis on the upper wall. Due to the presence of the stenosis, the height of the channel, δ, is a variable in the streamwise direction (i.e., $\delta = \delta(x)$) Away from the stenosis, the height of the pipe is a constant and is represented here using D (i.e., $\delta = D$ in the region either upstream or downstream of the stenosis). The stenosis is centered $5D$ downstream of the pipe inlet (i.e., the inlet location is $\delta/D = -5$) and $15D$ from the pipe outlet. The stenosis of the upper wall is centered at x/D= 0.0 and length of the stenosis is $2D$. The form of the stenosis chosen for this study is

$$\frac{y}{D} = 1 - \frac{f_c}{2}\left(1 - \cos\frac{x\pi}{D}\right), \qquad\qquad -D \le x \le D \qquad (2)$$

Where $f_c = \delta/D$ is a parameter that controls the height of the stenosis. In the present study, f_c is fixed to $3/4$, which results in a 75% reduction of the cross-sectional area at the center of the stenosis. Here we use x and y to represent the streamwise and radius respectively. We also use ξ_1 and ξ_2 to represent x and y respectively. The governing equation and momentum equations for an incompressible flow take the following forms in the general Cartesian curvilinear coordinate system

$$\frac{1}{|J|}\left(A_{11}\frac{\partial u}{\partial\xi_1} + A_{12}\frac{\partial u}{\partial\xi_2} + A_{21}\frac{\partial u}{\partial\xi_1} + A_{22}\frac{\partial u}{\partial\xi_2}\right) = 0 \qquad (3)$$

$$\rho\frac{\partial u}{\partial t} + \rho u\frac{1}{|J|}\left(A_{11}\frac{\partial u}{\partial\xi_1} + A_{12}\frac{\partial u}{\partial\xi_2}\right) + \rho v\frac{1}{|J|}\left(A_{21}\frac{\partial u}{\partial\xi_1} + A_{22}\frac{\partial u}{\partial\xi_2}\right) = -\frac{1}{|J|}\left(A_{11}\frac{\partial p}{\partial\xi_1} + A_{12}\frac{\partial p}{\partial\xi_2}\right)$$

$$+\left\{\begin{array}{l}\left(\frac{1}{|J|^2}\left[A_{11}^2\frac{\partial}{\partial\xi_1}\left(\mu\frac{\partial u}{\partial\xi_1}\right) + 2A_{11}A_{12}\frac{\partial}{\partial\xi_1}\left(\mu\frac{\partial u}{\partial\xi_2}\right) + A_{12}^2\frac{\partial}{\partial\xi_2}\left(\mu\frac{\partial u}{\partial\xi_2}\right)\right]\right) \\ +\left(\frac{1}{|J|^2}\left[A_{21}^2\frac{\partial}{\partial\xi_1}\left(\mu\frac{\partial u}{\partial\xi_1}\right) + 2A_{21}A_{22}\frac{\partial}{\partial\xi_1}\left(\mu\frac{\partial u}{\partial\xi_1}\right) + A_{22}^2\frac{\partial}{\partial\xi_1}\left(\mu\frac{\partial u}{\partial\xi_1}\right)\right]\right)\end{array}\right\} \qquad (4)$$

$$\rho\frac{\partial v}{\partial t} + \rho u\frac{1}{|J|}\left(A_{11}\frac{\partial v}{\partial\xi_1} + A_{12}\frac{\partial v}{\partial\xi_2}\right) + \rho v\frac{1}{|J|}\left(A_{21}\frac{\partial v}{\partial\xi_1} + A_{22}\frac{\partial v}{\partial\xi_2}\right) = -\frac{1}{|J|}\left(A_{11}\frac{\partial p}{\partial\xi_1} + A_{12}\frac{\partial p}{\partial\xi_2}\right)$$

$$+\left\{\begin{array}{l}\left(\frac{1}{|J|^2}\left[A_{11}^2\frac{\partial}{\partial\xi_1}\left(\mu\frac{\partial v}{\partial\xi_1}\right) + 2A_{11}A_{12}\frac{\partial}{\partial\xi_1}\left(\mu\frac{\partial v}{\partial\xi_1}\right) + A_{12}^2\frac{\partial}{\partial\xi_1}\left(\mu\frac{\partial v}{\partial\xi_1}\right)\right]\right) + \\ \left(\frac{1}{|J|^2}\left[A_{21}^2\frac{\partial}{\partial\xi_1}\left(\mu\frac{\partial v}{\partial\xi_1}\right) + 2A_{21}A_{22}\frac{\partial}{\partial\xi_1}\left(\mu\frac{\partial v}{\partial\xi_1}\right) + A_{22}^2\frac{\partial}{\partial\xi_1}\left(\mu\frac{\partial v}{\partial\xi_1}\right)\right]\right)\end{array}\right\} \qquad (5)$$

Where A_{11}, A_{12}, A_{21} and A_{22} are the elements of the cofactor matrix, **A** of the Jacobian $|J|$.

2.3. Numerical procedures:

The governing filtered equations (2-5) in Cartesian coordinates are transformed into curvilinear coordinates system and the finite volume approaches are used to discretised the partial differential equations to yield a system of linear algebraic equations. To discretise the spatial derivatives in eqns. (2-3), the standard second order accurate central difference scheme is used, expert for the convective terms in the momentum equations (3) for which an energy conserving discretisation scheme. Using the above mentioned pressure correction algorithm the computed pressure and the velocity components are stored at the center of a control volume according to the collocated grid arrangement. The Poisson like pressure correction equation is discretised by using the pressure smoothing approach, which prevents the even-odd node uncoupling in the pressure and velocity fields. A BI-CGSTAB [14] solver is used for solving the matrix of velocity vectors, while for the Poisson like pressure correction equation a ICCG [15] solver is applied due to its symmetric and positive definite nature. Overall the code is second order accurate in both time and space, which is in-house, developed.

3. Results and Discussion

The term stenosis can mention to an abnormal constriction of an artery, generally of a discrete segment. In the case of an artery, stenosis most commonly happens in large circulating arteries for example coronary, renal, cerebral, iliac and

femoral arteries. The narrowing commonly occurs from a chronic infection method - atherosclerosis. Sometimes a vessel can become acutely stenotic due to focal vasospasm. In general, stenosis takes place from chronic vascular disease. The term "**critical stenosis**" mentions to a critical narrowing of an artery (stenosis) that outcomes in an important decrease in maximal flow capability in a distal vascular bed. Critical stenosis normally is considered of in periods of a 60-75% decrease in the diameter of the large circulating artery. Fig.1 shows the schematic diagram of arterial stenosis in terms of 75% reduction of diameter. Here the diameter of artery is D and the length of stenosis region is 2D.
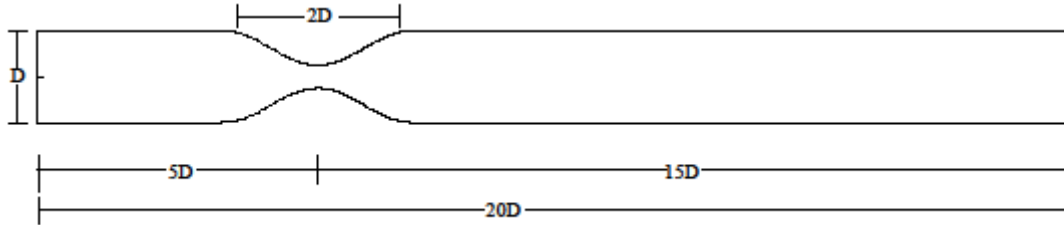

Fig1: Schematic diagram for the model arterial stenosis

Fig. 2(a) describes the wall pressure distribution. In this section, we are going to make you familiar with how pressure behaviour for pre and post stenotic region including the result of the stenotic point too. Here, the dotted line refers to non-Newtonian and the solid line refers to Newtonian case. As we see the graph from pre stenotic region to post stenotic region, we find a sudden acute drop at stenotic point for both cases. The Newtonian flow has a slightly larger drop than the non-Newtonian flow. When it starts reaching the downstream, it tries to recover from there. As a result, we can notice that it goes high quickly just after the peak drop point. In the Newtonian case, the flow fluctuates rapidly where as the non-Newtonian increases a moderate amount in the starting of the downstream region and then it goes steadily in a decreasing manner.
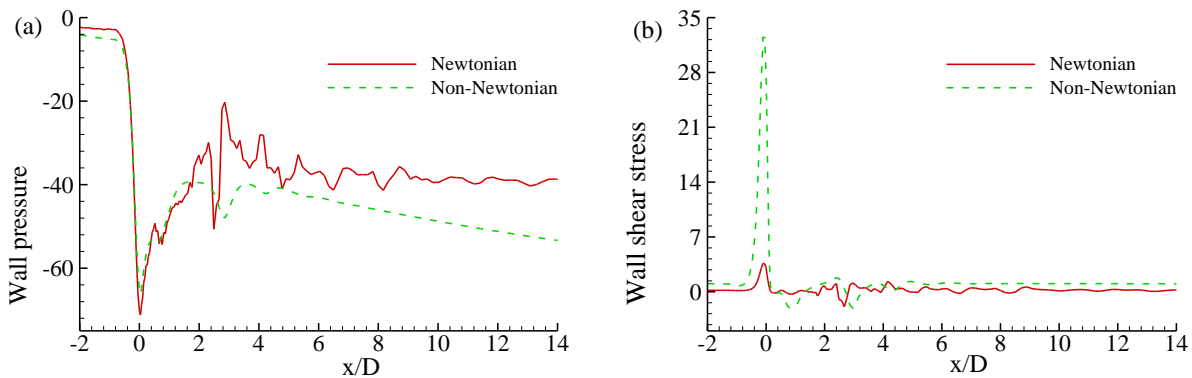

Fig 2: (a) Wall pressure, $p/\rho U^2$ and (b) wall shear stress, $\tau_w/\rho U^2$ for the Newtonian and non-Newtonian blood.

As we have seen earlier that wall pressure drop becomes high at the point of stenosis but different phenomena occur in case of wall shear stress distribution. Wall shear stress, another quantity of considerable physiological interest, is shown in Fig.2 (b). Where the dotted line corresponds to Non- Newtonian and the solid line corresponds to Newtonian cases. Furthermore, at the centre of the stenosis, the wall stress is maximum for both the Newtonian and Non-Newtonian cases. However, from the graph we can noticeably see that non- Newtonian wall share stress is very higher than Newtonian case at the stenosis place. However, both the figures show that when it goes far from stenosis non-Newtonian, wall share stress is steady and it gives a fixed value of wall share stress. On the other hand, Newtonian wall share stress fluctuates slightly. In this region, the wall stress increases sharply to reach a peak value and then from the point of the maximum it decreases rapidly in the reverse direction for the non- Newtonian case. Furthermore, Newtonian case shows a different result and it does not go as high as non Newtonian in this region; rather it moves slightly upstream and then behaves almost like a constant behaviour for rest of the region. Finally, it can be concluded that, the wall shear stress is significantly larger in the non-Newtonian case than the Newtonian case, which is an important factor in the medical issue.

In Fig 3(a)-(f), here we can observe the velocity of the Newtonian and non-Newtonian cases for six different axial locations. We start our simulation starting from the inlet (x/D = -5) and end with the outlet (x/D = 15) of the arterial segment. In between, we took four locations and those are velocities at position x/D (= 0, 2, 4, 6) which show the result in

Fig. 4(b), (c), (d) and (e) respectively. Fig 3 (a) is for inlet and (b) is for outlet. At the inlet of the artery, the velocity of both the cases seems to be same which has a nice parabolic shape and is symmetric about the axis of pipe. At inlet of artery the centre line velocity or pick velocity is approximately 2.7 but when it reaches the stenosis point, it increases significantly. In this position, the peak value is 11.6 approximately. Where the inlet peak was only 2.7 and Newtonian has a slightly greater
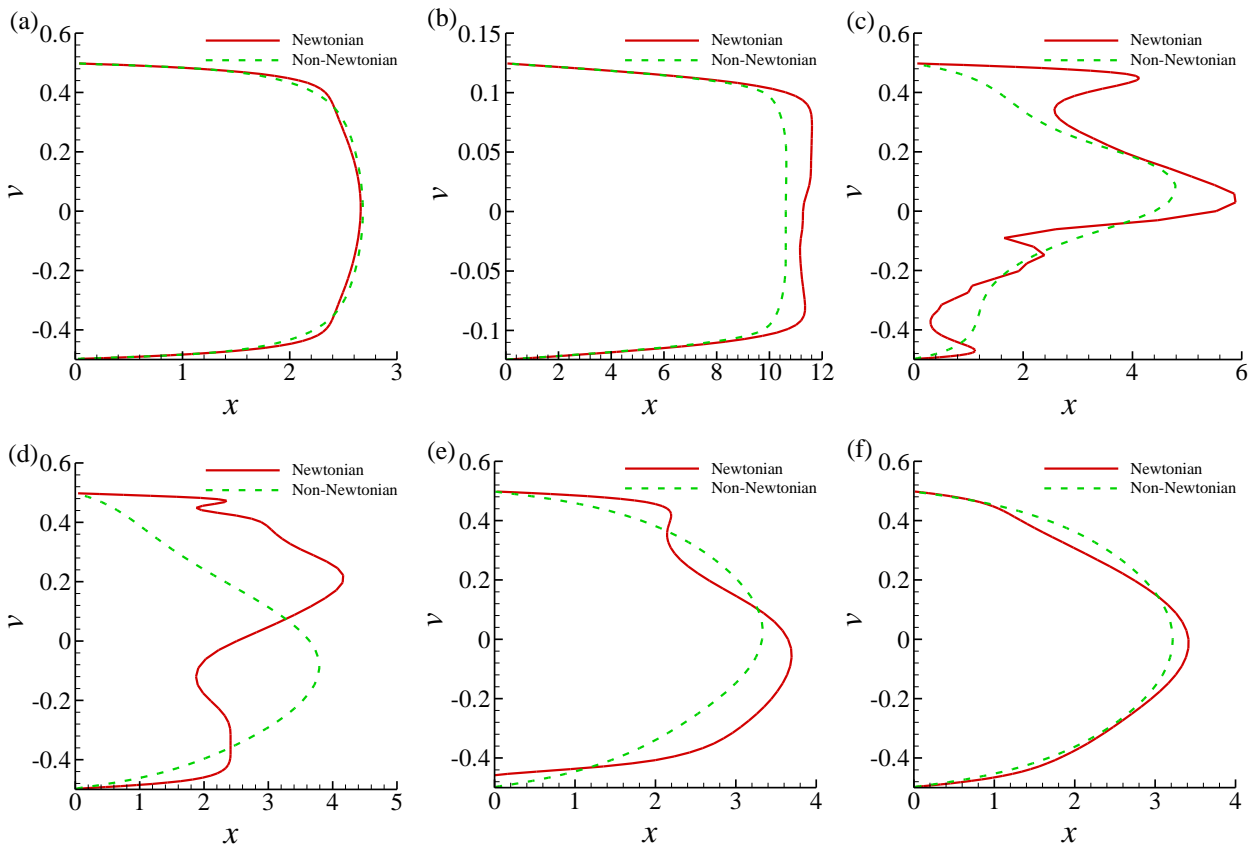

Fig 3: Streamwise velocity u/U, at the different axial position (a) inlet (b) h/D = 0.0, (c) h/D = 2.0, (d) h/D = 4.0, (e) h/D = 6.0 and (f) outlet at the time period t/T =10.25.
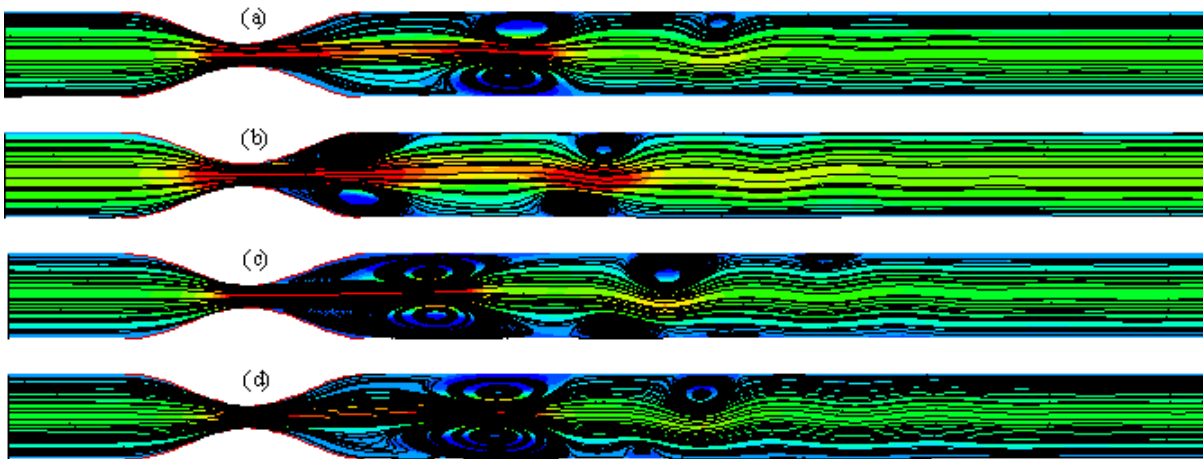

Fig.4: Streamlines for the non-Newtonian blood flow at the different pulsatile phase (a) t/T = 9.0, (b) t/T = 9.3, (c) t/T = 9.6 and (d) t/T = 9.9

value than Non-Newtonian fluid case. However, it still maintains its symmetric pattern. Phenomena start changing when the fluid enters to the post stenotic region. It loses its symmetric pattern and in Newtonian case does it quickly than Non-Newtonian case. This may happen because when the fluid passes through the stenotic point, there creates high vorticity and

then flow may becomes transitional. As a result, the frames (c) and (d) show a more chaotic result than the others. This state of velocity profile may call transient state because these two states can be distinguished easily from other states and from where it goes from one state to another. Frame (d) shows that Non-Newtonian figure is symmetric whereas the Newtonian figure is non symmetric because of Newtonian case, which carries high velocity than the Non-Newtonian. At the end, it passes the transient state to get back its steady and symmetric laminar velocity again by getting far from the stenosis.
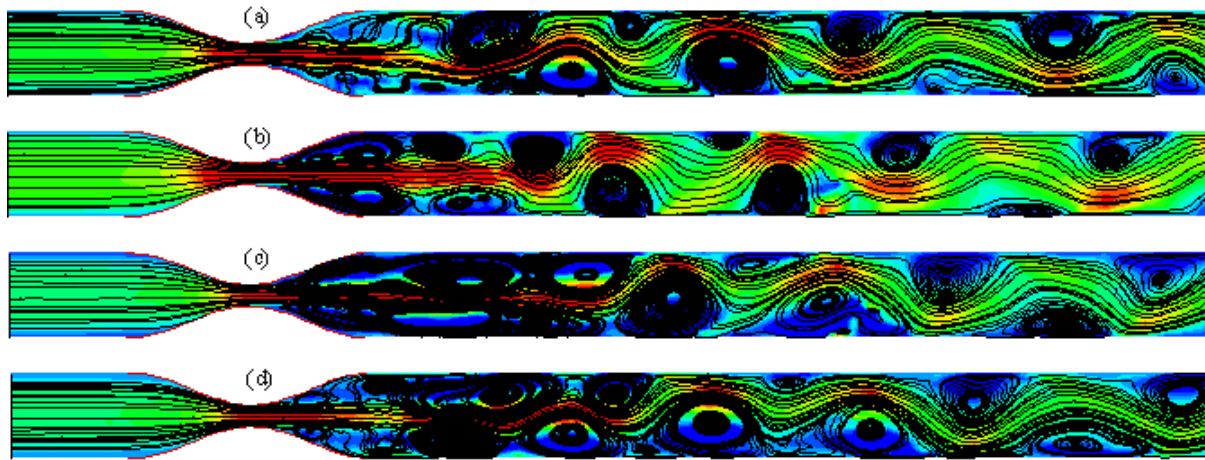

Fig. 5: Streamlines for the Newtonian blood flow at the different pulsatile phase (a) t/T = 9.0, (b) t/T = 9.3, (c) t/T = 9.6 and (d) t/T = 9.9.

Fig.4 (a) to (d) shows the streamlines for four different pulsatile phase for the Non-Newtonian case. Naturally, blood flow is unsteady due to heart pump and blood flows in a sinusoidal cyclic nature. The heart ejects and fills with blood in alternating cycles called *systole* and *diastole*. That is why these streamline diagrams drawn based on sinusoidal cycle and the each cycle range is from 0 to 2π. The 10th cycle of the simulation pulse is divided into four parts and presents some results by streamline at the different phase t/T (= 9.0, 9.3, 9.6 and 9.9) in Fig.4 (a)-(d), respectively. Whereas Fig. 5(a)-(d) represent same phase streamlines for the Newtonian case. In addition, if we pay attention to Fig. 5, we can examine the differences of vortex creation between (a) to (d). First of all, vortex creates a little bit far from the stenosis. Then it comes closer and increase a little as well. In the third part we find vortex stronger than others and at the end, it looks like the first situation in a stronger way. On the other hand, due to less viscous effect, transitional flow takes places quickly after stenosis in Newtonian phenomena. For the Newtonian case, the creation of vortex cell is higher than the Non-Newtonian case, because velocity of blood flow is very high in Newtonian case rather than Non-Newtonian case. in addition to this abnormal vortex is harmful in the point of pathological issue. Because of this vortex blood cannot flow properly and it takes time to reach its ultimate destination and this is the main reason of heart attack and brain stroke. Therefore, if we compare between Non-Newtonian and Newtonian case we can easily state that Newtonian case is very harmful for its high velocity.

3. Conclusion

Many studies have been undertaken experimentally and theoretically treating blood as Newtonian fluid. In this paper, blood is considered as Newtonian and non-Newtonian fluid and the simulation is done for Re = 300. Our main purpose is to find out how blood behaves in arterial stenosis when it is assumed as Newtonian and non-Newtonian fluid. For both the cases we found different results for different distribution like pressure, wall shear stress, velocity etc. In the case of shear stress and pressure, we found how pressure drops at stenosis and how its stress increases suddenly at the centre of the stenosis. In the case of Non-Newtonian blood the flow is always laminar whether a transient flow is observed in the post stenotic region in the Newtonian case. Also, at the centre of the stenosis the wall shear stress is very high which is harmful for the inner side of the arterial wall and at the post stenotic region the flow recirculation created due to the adverse pressure gradient.

References

[1] Ku, D.N., 1997. Blood flow in arteries, Annual Review of Fluid Mechanics 29, p. 399.
[2] Bharadvaj, B.K., Mabon, R.F., and Giddens, D.P., 1982. Steady flow in a model of the human carotid bifurcation. Part 1—flow visualization, Journal of Biomechanic 15(5), p. 349.

[3] Perktold, K., Resch, M., and Florian, H., 1991. Pulsatile non-Newtonian flow characteristics in a three-dimensional human carotid bifurcation model, Journal of Biomechanical Engineering 113, p.464.

[4] Perktold, K., Thurner, E., and Kenner, T., 1994. Flow and stress characteristics in rigid walled and compliant carotid artery bifurcation models, Medical & Biological Engineering & Computing 32, p.19.

[5] Chien, S., 1981 Hemorheology in clinical medicine, Recent Advances in Cardiovascular Diseases **2** (Suppl.), p.21.

[6] Deplano, V., Siouffi, M., 1999. Experimental and numerical study of pulsatile flows through stenosis: Wall shear stress analysis, Journal of Biomechanics 32, p.1081.

[7] Giddens, D.P., Zarins, C.K., Glagov, S., 1990. Response of arteries to near wall fluid dynamic behaviour, Applied Mechanics Review 43 (2), p.S98.

[8] Bereger, S. A., Jou, L. D., 2002, Flows in stenotic vessels, Annual Review of Fluid Mechanics, 32, p. 347-382.

[9] Fry, D.L., 1969. Certain histological and chemical responses of the vascular interface to acutely induced mechanical stress in the aorta of the dog, Circulation Research. 24, p.93.

[10] Crao, C.G., Fitzgerald, J.M., and Schroter, R.C., 1971. Atheroma and arterial wall shear observations, correlation and proposal of a shear dependent mass transfer mechanism for atherogenesis. Proceeding of the Royal Society London Series B, 17(7), p.109.

[11] Ku, D.N., Giddens, D.P., Zarins, C.K., and Glagov, S., 1985. Pulsatile flow   and atherosclerosis in the   human carotid bifurcation, Arteriosclerosis 5(3), p.293.

[12] Lie, M., Kleinstreuer, C., and Truskey, G.A., 1995. Numerical investigation and prediction of atherogenic sites in branching arteries, Journal of Biomechanical Engineering 117, p.350.

[13] Cross, M. M. 1965, Rheology of non-Newtonian fluids: a new flow equation of viscoelastic fluids, Journal of colloid Science, 20, p. 417-437.

[14] Kershaw, D. S., 1978. "The incomplete cholesky conjugate gradient method for the iterative solution of systems", Journal of Computational Physics 26, p.43.

[15] Vorst, H. A. D., 1992. "BI-CGSTAB: a first and smoothly converging variant of BI-CG for the solution of the non-symmetric linear systems", SIAM Journal on Scientific and Statistical Computing 155, p. 631.

Appendix

. In this paper governing Navier-Stokes equations have been modified using the Cartesian curvilinear coordinates to handle the complex geometry such as arterial stenosis. For this reason we use Jacobian matrix to simplify our complex geometry.

$$
|J| = \begin{vmatrix} \dfrac{\partial x_1}{\partial \xi_1} & \dfrac{\partial x_1}{\partial \xi_2} \\ \dfrac{\partial x_2}{\partial \xi_1} & \dfrac{\partial x_2}{\partial \xi_2} \end{vmatrix} \qquad \text{or} \qquad |J| = \frac{\partial x_i}{\partial \xi_j} A_{ij} \qquad (1)
$$

Where $A_{11} = \dfrac{\partial x_2}{\partial \xi_2}$, $A_{12} = \dfrac{\partial x_2}{\partial \xi_1}$, $A_{21} = \dfrac{\partial x_1}{\partial \xi_2}$ and $A_{22} = \dfrac{\partial x_1}{\partial \xi_1}$ are the elements of the cofactor matrix**, A** , of the

Jacobian $|J|$.And $J_{ij} = \dfrac{\partial x_i}{\partial \xi_j}$; where $J_{ij} \rightarrow$ elements of Jacobian matrix.

5th BSME International Conference on Thermal Engineering

Numerical Study of the Effect of Wedge Angle of a Wedge-Shaped Body in a Channel Using Lattice Boltzmann Method

M.A.Taher[a]*,Y.W.Lee[b], H.D.Kim[c]

^{a}Department of Mathematics, Dhaka University of Engineering & Technology, Gazipur, Bangladesh
^{b}School of Mechanical Engineering, Pukyong National University, Busan, Korea
^{c}School of Mechanical Engineering, Andong National University, Andong, Korea

Abstract

The aim of this paper is to study the fluid flow behavior around a wedge shaped body with different wedge angles placed in a channel using Lattice-Boltzmann Method (LBM). The LBM has built up on the D2Q9 model and the single relaxation time method called the Lattice-BGK (Bhatnagar-Gross-Krook) model. The influence of the gap ratio $G^*=G/H$, where H is the distance between two parallel walls, G is the gap between body and wall, on the flow field is illustrated. The gap ratio, G*, depends on the angle of wedge-shaped body ($0^0 < \theta < 180^0$). Streamlines, vorticity contours and pressure contours are provided to analyze the important characteristics of the flow field for a wide range of non dimensional parameters namely the Reynolds number (Re), Strouhal number (St) and the gap ratio(G^*). However, it is seen that the flow can be characterized by three regions: (i) large gap ratio, $0.44 < G^* < 0.50$, with $0^0 < \theta < 55^0$, (ii) intermediate gap ratio, $0.20 \leq G^* \leq 0.44$, with $55^0 \leq \theta \leq 120^0$ and (iii) small gap ratio, $0 < G^* < 0.20$, with $120^0 < \theta < 180^0$. The simulation results are compared with experimental data and other numerical models and found to be very reasonable and satisfactory.

Keywords: Lattice-Boltzmann, Bhatnagar-Gross-Krook, Reynolds number, Strouhal number, Wedge-shaped, Gap ratio.

Nomenclature

C_p	Specific heat at constant pressure (J.kg^{-2} K^{-1})
Cs	Speed of sound (m.s^{-1})
c	CFL number
e_i	Discrete particle velocity vector (m s^{-1})
F_i	Discrete particle distribution function
F_i^{eq}	Discrete particle distribution function
f	*S*hedding frequency
G	Gap between body and wall (m)
G^*	Gap ratio
H	Channel height (m)
L	Channel length (m)
Re	Reynolds number

* Corresponding author. M. A. Taher, Tel.: 880-1614619094
E-mail: tahermath@yahoo.com

St	Strouhal number
U	Characteristic velocity (m.s^{-1})
u, υ	Fluid velocity in x and y direction respectively(m.s^{-1})
w_i	Weighting factor
Greek symbols	
τ	Relaxation parameter for momentum
ρ	Density of the fluid (kg m^{-3})
μ	Viscosity of the fluid (kg m^{-1} s^{-1})
β	Coefficient of wedge angle
v	Kinematic viscosity (m^2 s^{-1})
ω	Relaxation parameter
θ	Wedge angle
Abbreviations	
BGK	Bhatnagar-Gross-Krook
CFD	Computational fluid dynamics
CFL	Courant-Friedriehs- Lewy
D2Q9	2D-9 velocities
LBM	Lattice-Boltzmann Method
N-S	Navier-Stokes
PDF	Particle distribution function

1. Introduction

In the past years, the Lattice Boltzmann Method (LBM) has attracted much attention as a novel alternative to traditional computational fluid dynamics(CFD) methods for numerically solving the Navier–Stokes (N-S) equations. Actually the LBM originated from the Lattice Gas Automata (LGA) method, which can be considered as a fictitious molecular dynamics (MD) in which space, time and particle velocities are all discrete. Lattice gas models with an appropriate choice of the lattice symmetry in fact represent numerical solutions of the Navier-Stokes equations and therefore able to describe the hydrodynamics problems have been discussed by McNamara et .al [1] and Wei et al. [2]. Due to the sampling of the particle velocities around zero velocity, LBM is limited to the low Mach number (nearly incompressible flow) flow simulation. It is commonly recognized that the LBM can faithfully be used to simulated the incompressible Navier-Stokes (N-S) equations with high accuracy and this lattice BGK (LBGK) model, the local equilibrium distribution has been chosen to recover the N-S macroscopic equations by different authors [3-5]. It is found that the simulation results from LBM are in good quantitative agreement with experimental results. However, He and Luo [6] shown that the lattice Boltzmann equation is directly derived form the Boltzmann equation with various approximations by discretization in both space and time. In their study, they demonstrated that simulation results from LBM are in good quantitative agreement with experimental results. An overview of LBM, a parallel and efficient algorithm for simulating single-phase and multiphase fluid flows and also for incorporating additional physical complexities have been discussed by Chen and Doolen [7]. Taher and Lee [8] have investigated numerically the suppression of fluid forces acting on a bluff body with different control bodies. It is found that the fluid forces acting on the main bluff body are effectively suppressed if the control body (a thin plate or a small circular cylinder) is placed at a suitable position with proper height or diameter. Moreover,LBM has several advantages over other conventional CFD methods, especially in dealing with complex boundaries, incorporating of microscopic interactions, and parallelization of the algorithm that are described in the excellent books by authors [9-12]. The viscous flow past a bluff body and the resulting separated region behind it has been focus on numerous experimental and numerical investigations. There is no doubt that an enormous corpus of literature on the subject of bluff body wakes has developed since the pioneering work of Strouhal and Von Karman. This flow situation is popular not only because of its academic attractiveness but also owing to its related technical problems associated with energy conservation and structural design. This type of flow is of relevance for many practical applications, e.g. vortex flow meter, buildings, bridge, towers, masts and wires. A laminar vortex shedding region is known to occur for the Reynolds number range extending approximately from 50-80 and the universal relationship between Reynolds and Strouhal numbers around a circular cylinder have been studied by and Williamson [13]. Actually many authors have been studied the vortex shedding frequency behind a circular cylinder or square cylinder or two cylinders for different cases both in numerically and experimentally However, in this paper, the present authors want to study the fluid flow behaviors around wedge-shaped using lattice Boltzmann method (LBM).As far we know, the problem has not been considered before. The objective of this paper is to numerically study of fluid flow behavior around wedge-shaped body using LBM where flow can be driven with the pressure (density) gradients. Computations are carried out for various wedge angles ranging from 0^0 to 180^0 and the Reynolds number ranging from 0 to 397, based on the characteristic length of the channel, the maximum incoming flow velocity (less than 0.1 lu) and also the nature of fluid transport

properties. Here we have focused our attention on the evolution of streamlines, vorticity contours, pressure contours as well as velocity profiles and vortex shedding frequency, to investigate the important characteristics of the flow field around wed-shaped body for a wide range of non-dimensional parameters that present in our simulation namely Reynolds number (Re), Strouhal number (St) and Gap ratio (G*). Throughout our calculation, we use Lattice-Boltzmann units.

2. Formulation of the problem

The computational domain is to consider as a rectangular region $L{\times}H$, where H is the height and L= 4H is the length of the channel. A wedge-shaped body having wedge angle θ placed symmetrically between parallel walls as shown in Fig.1
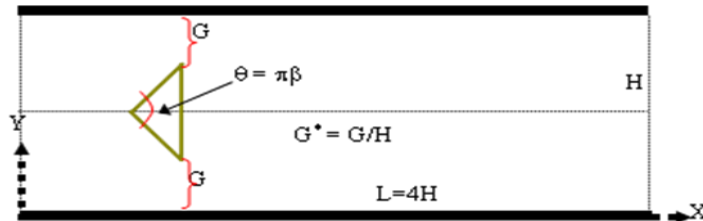

Fig.1. Physical model and coordinate systems.

The wedge angle is defined by $\theta = \pi\beta$, $0 \leq \beta \leq 1$. It is noted that, in the case of β equal to zero corresponds to flow over a horizontal flat plate while β equal to 1.0 corresponds to flow over a vertical flat plate. So the angle measurement is very important in this analysis. If G is the gap between wall and the body then $G^* = G/H$ is defined as a gap ratio. It is noted that if the value of β increase, then G^* decreases. For convenient, it has been discussed in the present study of the following three different cases.

Table 1. The different cases of wedge-shaped body:

	β	θ	$G^*(=G/H)$
Case 1	0.25	45^0	0.45
Case 2	0.50	90^0	0.375
Case 3	0.75	135^0	0.20

In an incompressible flow, Reynolds number is the only parameter that controls the flow field and is define by Re=UD/v, where U and D are the characteristic velocity and the length respectively. In fluid dynamics, vorticity is the circulation per unit area at a point in the flow field. Mathematically, it is defined as, $\vec{w} = \nabla \times \vec{u}$, where $\vec{u}$ is the fluid velocity. The non dimensional shedding frequency, the Strouhal number, is defined as: St = fD/U, where f is the vortex shedding frequency. This relation is believed to be accurate to ±1% in the Reynolds number. In this section, it is assumed that, $\Delta x = 1 lu = 1.27 \times 10^{-6}$ m, $\Delta t = 1$ $ts = 2.44 \times 10^{-9}$s. The fluid properties are taken to air properties. The kinematic viscosity v =15.636$\times 10^{-6}$ m²/s, which corresponds to 0.024 lattice unit. All reported data are obtained on our calculation domain 320× 80 (lattice node). Thus the physical domain of simulation is 400 μm ×100 μm. For accurate solution, the Mach number, Ma, should be kept as small as possible. In general, the maximum incoming fluid velocity U is considered in the LBM in order of 0.2 or 0.1 or less. Therefore, the Reynolds number should be chosen very carefully.

In order to simulate a fully developed laminar channel flow upstream of the wedge-shaped body, a parabolic velocity profile can be used with a maximum velocity U at the midpoint of the channel. This velocity is chosen to be lower than 10% of the speed of sound for LBM simulations to avoid significant compressibility effects. In our simulation, we use Zou-He Boundary condition to implement Dirichlet boundaries on inlet/outlet. At the top and bottom wall, no slip boundary conditions were imposed by the standard bounce back treatment. In LBM, the movement of the fluid particles is modeled instead of directly solving the macroscopic fluid quantities like the velocity and the pressure. It is known as mesoscopic simulation model, which is based on the Boltzmann equation. Neglecting external forces, the Boltzmann equation (BE) with BGK approximation can be written as

$$\frac{\partial F_i}{\partial t} + e_i \cdot \frac{\partial F_i}{\partial \vec{x}_i} = -\frac{1}{\tau}(F_i - F_i^{eq}) \ , \quad \text{i} = 0,1,2,3........, q\text{-}1 \tag{1}$$

Where, $F_i(\vec{x},t)$ is the discrete particle distribution function and F_i^{eq} is the discrete equilibrium distribution function at lattice

position $\vec{x}$ and time t defined by

$$F_i^{eq} = \rho w_i [1 + \frac{3}{c^2} \vec{e}_i.\vec{u} + \frac{9}{2c^4} (\vec{e}_i.\vec{u})^2 - \frac{3}{2c^2} u^2]$$

(2)

The lattice weighting factors, w_i, depend on the lattice model. For D2Q9 model, each node of the lattice has three kinds of particle: a rest particle that resides in the node, particles that move in the co-ordinate directions and the particles that move in the diagonal directions. So the total number of discrete velocities (e_i) on each node in D2Q9 model is 9.

Table 2. D2Q9 lattice velocities.

$e_0 = (0, 0)$	$e_1 = (c, 0)$	$e_2 = (0, c)$	$e_3 = (-c, 0)$	$e_4 = (0, -c)$
$e_5 = (c, c)$	$e_6 = (-c, c)$	$e_7 = (-c, -c)$	$e_8 = (-c, c)$	

Here c is called the Courant-Friedrichs- Lewy (CFL) number and is proportional to $\Delta x/\Delta t$, where Δx and Δt are the lattice space and the time steps respectively. Therefore the discrete form of equation (1) is called the Lattice- Boltzmann equation (LBE) and can be defined as

$$F_i(\vec{x} + \Delta t \, \vec{e}_i, t + \Delta t) - F_i(\vec{x}, t) = -\frac{1}{\tau}(F_i - F_i^{eq}), \quad i = 0, 1, 2, ----------, 8$$

(3)

The relaxation parameter, $\omega = 1/\tau$, depends on the local macroscopic variables ρ and $\rho \vec{u}$. These variables should satisfy the following laws of conservation:

$$\rho = \sum_i F_i \quad , \quad \rho \vec{u} = \sum_i \vec{e}_i \, F_i$$

(4)

The above expressions describe the relationships between the microscaled quantities and the macro scaled physical quantities. Using the Chapman-Enskog expansion, i.e. multi-scale analysis, it is mathematically provable that the LBM equation (3) can recover the N-S equation to the second order of accuracy in the limit of low Mach number [5], if the pressure and the kinetic viscosity are defined by $P = \rho Cs^2$ and $\nu = (\tau-1/2) Cs^2 \Delta t$.

3. Results and discussions

In this problem, equation (3) is an algebraic equation. In conventional CFD methods for incompressible N-S equations, we need to solve the Poisson equation for the pressure, while in LBM, solving the equation (3) we get all information that we interested to our study. In Fig.2, we compare our result with analytical solution for Re =100, 200 in a channel in order to assess the accuracy of our method.
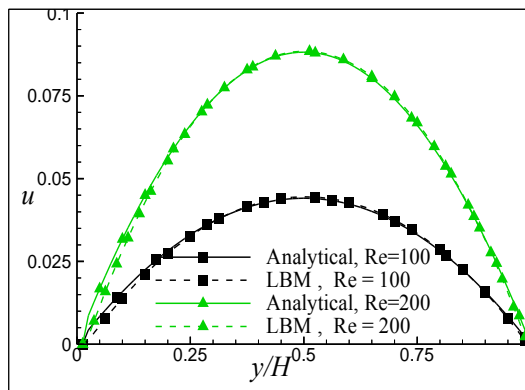

Fig.2. Verify LBM with analytical result for different Reynolds numbers

The solid lines are the analytical solution and the dashed lines are the data results obtained from the simulation. This figure shows that the velocity profile in the channel is parabolic and the maximum value at the middle position of the channel. It is obviously as we consider the fully developed laminar parabolic flow and it is seen that our results are in excellent agreement with analytical solution. This confirms the accuracy of our present simulation. One important quantity taken into account in the present study is the Strouhal number(St = fh/U)), computed from the height (h) of the bluff body,

the vortex shedding frequency (f) and the velocity of the incoming fluid. The dimensionless shedding frequency with Reynolds number along the wake centerline downstream of the wedge-shaped body is shown in Fig.3
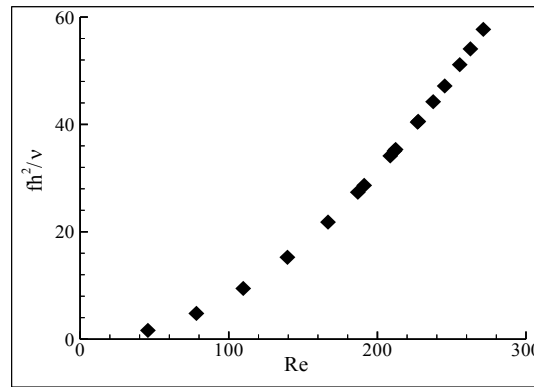

Fig.3.Variation of dimensionless shedding frequency with Reynolds number

It is noted that the flow velocity profile, the position, shape of the bluff (barrier) and the ratio of the cross section area of the bluff to the wall affect the Strouhal number(St) for the given Reynolds number(Re) of the flow regime. As the dimensionless vortex frequency increases when the gap ratio decreases with the Reynolds number in the range 45-275 and consequently the Strouhal number also increases within this range. The higher frequency means that the process of vortex shedding is faster. Therefore, the nature of the vortex shedding is a strong function of the Re. In order to gain further insight into the evolution of vortex shedding in the near-weak region, the patterns of the vorticity contours for Re=100, 200 and 300 with different gap ratios are plotted in Figs. 4-6.
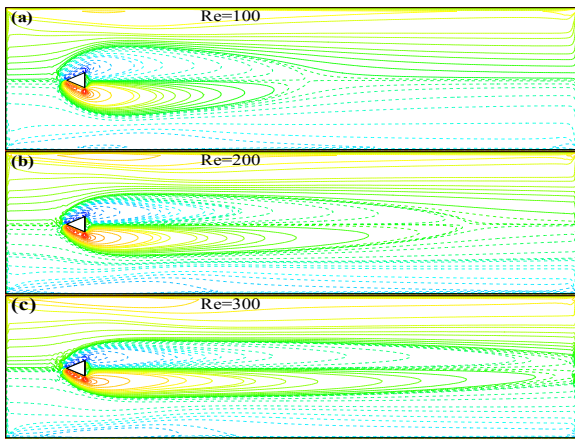

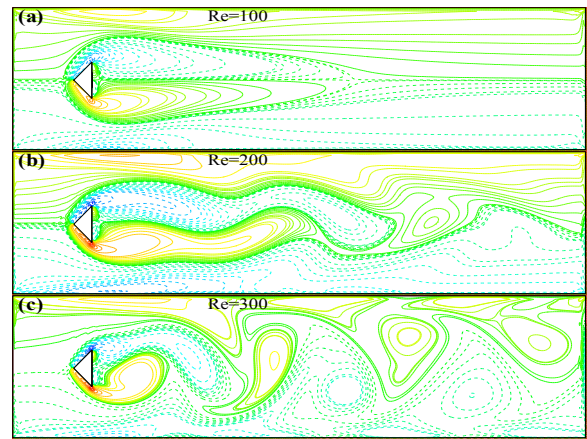

Fig.4.Vorticity distribution for $\theta = 45^0$ with Re
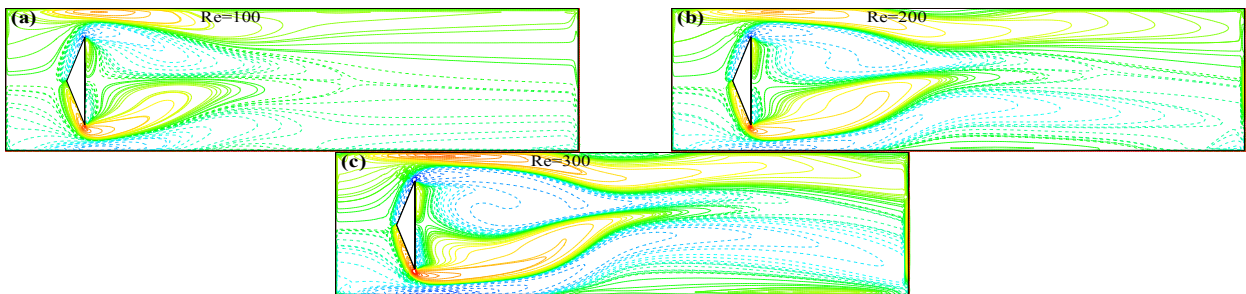
Fig.5.Vorticity distribution for $\theta = 90^0$ with Re

Fig.6.Vorticity distribution for $\theta = 135^0$ with Re

For small wedge angle, higher gap ratio, it is seen that a pair of vortices with same strength and size are formed behind the body; a positive vortex (anticlockwise) appears on the lower part of the body and a negative vortex (clockwise) on the

upper part of the body. Further, It is observed that for low wedge angles ($< 55^0$), the flow patterns are almost symmetrical for all Reynolds number within the range up to 300. However, for large wedge angles, an unsymmetrical flow patterns have been seen around the body as shown in the Fig.5-6. For, $\theta = 90^0$ with Re < 195, the fluid flow behaviors is almost symmetric. Moreover, a significant changed in the flow is observed when Re $\geq$ 195. In Fig. 5(b)-(c), the Von Karman Street is seen, which is consists of vortices in a regular arrangement. For Re=200, the width of the vortex street behind the body is narrower compare to the Re = 300. The width is increasing with the increasing of Reynolds number. When Re $\geq$ 230, the strong vortices are observed i.e. the width of the vortex street and the numbers of vortices are remarkably changed. There are seven vortices are seen in Fig.5(c) within the considered wake region for Re=300. This kind of flow behaviors are observed with the wedge angles in the range of $55^0 \leq \theta \leq 120^0$. Further, the increases in the wedge angle (Fig.6) correspond to very low gap ratio, a pair of vortices are formed just behind the body, and in addition, the wall proximity effects are seen to give rise to reverse Von Karman Street.
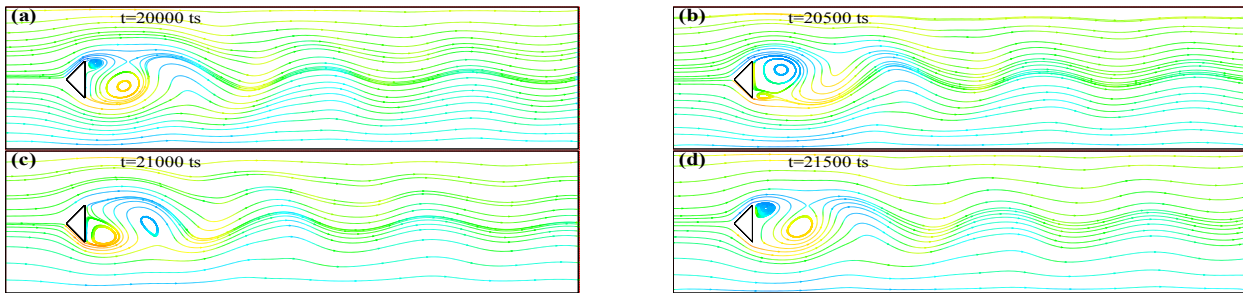

Fig.7. Streamlines plot for different time steps with Re = 260 and $\theta = 90^0$.

A detailed view of flow field behind the wedge-shaped body and changes in the vortex shedding pattern with different time steps are shown in Fig.7. The flow is developed until 20,000 time steps. In Fig.7 (a), a new vortex is forming on the top of the body but the lower one is pulled away from the body. The formation of the upper vortex is completed at 20,500 time steps and consequently another new vortex on the bottom is forming and it is observed that the vortices are shed alternately with different time steps. Finally, the last plot, at time steps t = 21500, is nearly identical with the Fig.7 (a). This evolutionary process is repeated approximately every 1500 time steps. This time period is strongly depends on the Reynolds number. If the Reynolds number increases, the time period becomes shorter. It is investigated that for Re=300, the time period is approximately 1000 time steps. The same phenomenon has been seen that for flow over an airfoil at -90 degrees angles of attack documented by Rogers and Kwak [14].
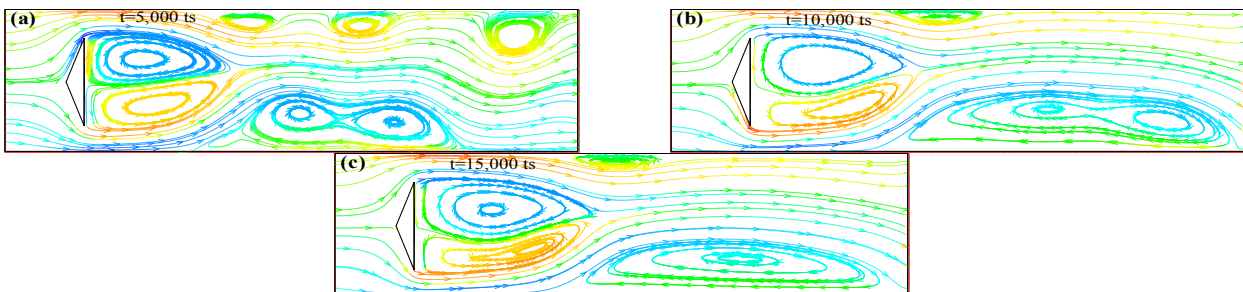

Fig.8. Streamlines plot for different time steps with Re=300, $\theta =135^0$

Typical examples of instantaneous flow fields are presented in terms of vorticity for various time steps with wedge angle, $\theta =135^0$, corresponding to the gap ratio $G^* = 0.20$. This is easily understood by examining streamlines shown in Figs.8 (a)-(c). At t = 5,000 time steps, two opposite vortices with almost similar size and shape are seen just behind the body and simultaneously three stationary vortices are seen on the top wall whereas two vortices are seen on the bottom wall of the channel. The recirculation regions on the bottom wall are much larger than those of top wall. In Fig.8 (b), the upper vortex just behind the body a little extended and the two stationary vortices on the top wall far from the body are merging but the one (near the body) is still observed. However, the two vortices at the bottom wall have shown to tendency to become a large one. Finally, at t = 15,000, the two vortices on the bottom wall converted to one big size vortex with same center. After t =15,000 times steps, there is no changed of the flow field. Thus it is concluded that, for higher wedge angle, small gap ratios, the change of flow field occurred until approximately 15,000 time steps. However, the flow separation on the wall is observed in this case. This phenomenon is observed when Re $\geq$ 130.
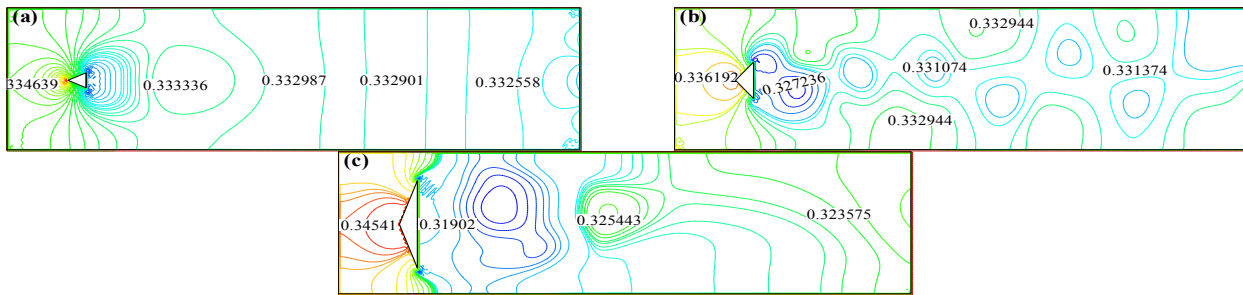
Fig. 9. Pressure fields for different wedge angles

Apart from the velocity profile, pressure distribution is important to understand the flow field behavior around the bluff body. Fig.8 shows the pressure contours with Reynolds number Re=300 for different angles $\theta = 45^0$, 90^0 and 135^0. In all cases, the pressure contour at the frontal stagnation point has maximum value where as just behind the body has minimum. Fig.9 (a), for large gap ratio, the variations of the pressure contours are not significant because the recirculation regions as well as the flow in the wake are fully developed. However, if the wedge angle increases, Figs.9 (b), the pressure contours becomes more complicated patterns and many recirculation regions are observed. The pressure contours indicate the location of vortex contours, where the pressure has a local minimum value. Further increased the wedge angle, Fig.9(c), corresponds to very low gap ratio, the wall effects are considerable. Therefore, there exist a little recirculation region and the variation of pressure contours are not significant at the far from the body. The same characteristic has found in Fig.6.

4. Conclusions

In this study, the flow can be characterized by three regions: (i) large gap ratio, $0.44 < G^* < 0.50$, with $0^0 < \theta < 55^0$, (ii) intermediate gap ratio, $0.20 \leq G^* \leq 0.44$, with $55^0 \leq \theta \leq 120^0$ and (iii) small gap ratio, $0 < G^* < 0.20$, with $120^0 < \theta < 180^0$. The investigations of these regions are as follows:

● For case 1, $\theta = 45^0$, the flow is almost symmetrical.

● For case 2, $\theta = 90^0$, the flow behind the body is characterized by a Karman vortex street when Re≥ 195 and the vortices become stronger with increasing the Reynolds number. The formation and the shedding of vortices are repeated during a time period. This time period becomes shorter with increasing the Reynolds numbers. For Re=260, the time period is approximately 1500 times steps (lattice unit) where as for Re=300, it is seen approximately 1000 time steps. This kind of flow behaviors are observed with the wedge angles in the range of $55^0 \leq \theta \leq 120^0$.

● For case 3, $\theta = 135^0$, the wall proximity effects are observed to give rise to reverse Von Karman street and consequently a packet of vortices are created on the both channel walls and it is observed when Re ≥ 130.

References

[1] McNamara, GR., Zanetti, G., 2004. Use of the Boltzmann equation to simulate lattice-gas automata. Physical Review Letters 61, pp. 2332-2335.
[2] Wee, X., Mueller, K., Kaufman, A E., 2004. The lattice Boltzmann method for simulating gaseous Phenomena. IEEE Transactions on Visualization and computer Graphics10 (2), pp. 164-176.
[3] Frishch, U., Hasslacher, B., Pomeau, Y., 1986. Lattice-gas automata for the Navier-Stokes equation. Physical Review Letters 56, pp. 1505-1508.
[4] Qian, Y H., D'Humieres, D., Lallemand, P., 1992. Lattice BGK models for Navier-Stokes equation. Euro physics Letter17 (6), pp. 479-484.
[5] Chen, H., Chen, S., Matthaeus, WH., 1992. Recovery of the Navier-Stokes equations using a lattice-gas Boltzmann method. Physical Review A 45(8), pp. 5339-5342.
[6] He, X., Luo, L S., 1997. Theory of the lattice Boltzmann method: From the Boltzmann equation to the lattice equation. Physical Review E 56(8), pp. 6811-6817.
[7] Chen, S., Doolen, G.D., 1998. Lattice Boltzmann method for fluid flows. Annu. Rev. Fluid Mechanics 30, pp. 329-364.
[8] Taher, M. A., Lee, Y.W., 2012. Numerical study on reduction of fluid forces acting on a circular cylinder with different control bodies using Lattice-Boltzmann method. Int. J. Energy and Technology 4(18), pp.1-7.
[9] Succi, S., 2001. The lattice Boltzmann equation for fluid dynamics and beyond. Oxford University press, UK.
[10] Wolf-Gladrow, D.A., 2005. Lattice gas cellular automata and lattice Boltzmann models: An introduction, Springer, Berlin.
[11] Suukop, M.C., Thorne, D.T., 2006. Lattice Boltzmann modeling, An introduction for geoscientist and engineering. Springer, Heidelberg
[12] Taher, M.A., 2009. Fluid flow and heat transfer analysis of pure and nanofluids using Lattice-Boltzmann method, Ph.D Thesis, Pukyong National University, Busan, Korea.
[13] Williamson, C.H.K., 1998. Defining a universal and continuous Strouhal-Reynolds number relationship for a laminar vortex shedding of a circular cylinder. Physics of Fluid 31(10), pp. 2742-2744.
[14] Rogers, S.E., Kwak, D., 1990. Upwind differencing scheme for the time-accurate incompressible Navier-Stokes equations. AIAA Journal 28(2),pp. 253-262.

5th BSME International Conference on Thermal Engineering

The Effects of Magnetic Field on the Fluid Flow through a Rotating Straight Duct with Large Aspect Ratio

Md. Kamruzzaman[a], Mohammad Wahiduzzaman[b], Md. Mahmud Alam[b] and Lyazid Djenidi[a], *

[a]Department of Mechanical Engineering, The University of Newcastle, Newcastle-2308, Australia
[b]Mathematics Discipline, Khulna University, Khulna-9208, Bangladesh

Abstract

This paper presents a numerical study of an investigation of a fluid flow through a rotating rectangular straight duct in the presence of magnetic field. The straight duct of rectangular cross-section rotates at a constant angular velocity about the centre of the duct cross-section is same as the axis of the magnetic field along the positive direction in the stream wise direction of the flows. Numerical calculation is based on the Magneto hydrodynamics incompressible viscous steady fluid model whereas Spectral method is applied as a main tool. Flow depends on the Magnetic parameter, Dean number and Taylor number. One of the interesting phenomena of the fluid flow is the solution curve and the flow structures in case of rotation of the duct axis. The calculation are carried out for $5 \leq M_g \leq 50000$, $50 \leq T_r \leq 100000$, $D_n = 500$, 1000, 1500 and 2000 where the aspect ratio $\gamma = 3.0$. The maximum axial flow will be shifted to the centre from the wall and turn into the ring shape under the effects of high magnetic parameter and large Taylor number whereas the fluid particles strength is weak.

Keywords: Magnetic parameter, Taylor number, Dean number and aspect ratio

Nomenclature	
γ	Aspect ratio
M_g	Magnetic parameter
D_n	Dean number
T_r	Taylor number
Q'	Dimensional total flow
Q	Non-Dimensional Total flow

1. Introduction

Fluid flows in a straight duct are of great importance. It has large applications in chemical and mechanical engineering. The purpose of this paper is to make some numerical calculations on the fluid flow through a rotating rectangular straight duct in the presence of magnetic field which has been interested to the engineering communication. The results of this

* Corresponding author. Tel.:+62-04132681792; fax: +0-000-000-0000 .
*E-mail address:*zaman9208@gmail.com; alam_mahmud200@yahoo.com

investigation may not have direct practical applications but are relevant to the problems mentioned above. The fluid flows through a rectangular straight duct to rotate at a constant angular velocity about an axis normal to a plane. Such rotation passages are used in cooling systems for conductors of electric generators. The earliest work on the flow in rotating straight pipe was carried out for the asymptotic limits of weak and strong rotations by Barua [2]. Benton and Baltimore [3] used a perturbation expansion to the Hagen-Poiseuille flow. Ito and Nanbu [4] and Alam, et al. [1] have used spectral method to describe the flow through a rotating straight pipe with large aspect ratio. MHD flow in an insulating rectangular duct under a non-uniform magnetic field is studied by [5]. Numerical simulations of MHD flows past obstacles in a duct under externally applied magnetic field is studied by [6]. [7] Investigates the study of surface and bulk instabilities in MHD duct flow with imitation of insulator coating imperfection. [8] Investigates the natural convective flow phenomena under the influence of magnetic field. [9] studied the rotational MHD flow field of unity magnetic Prandtl number in the effects of regional magnetic field. [10] has been observed the stability of viscous flow between rotating cylinders in the presence of a magnetic field.

Hence our aim is to study through the direct numerical simulation, the response of the magnetic effects on the fluid flow through a rotating rectangular straight duct with large aspect ratio**.**

2. Governing Equations

The fully developed laminar flow of an incompressible viscous fluid in a straight duct that is subjected to a steady rotation Ω with rectangular cross-section in the presence of magnetic field has been considered. Let $2a$ be the width of the duct cross-section and $2b$ its height. Cartesian co-ordinate system (x', y', z') has been considered to describe the motion of the fluid particles in the duct with the center O at the centralism of the rectangular cross-section duct as illustrated in Figure 1. The system rotates at a constant angular velocity $\Omega = (0, -\Omega, 0)$ around the

$y' -$ axis. The flow is derived by the pressure gradient $-\dfrac{\partial p}{\partial z} = G$ along the centerline of

the duct in the presence of magnetic field. u', v', w' are the dimensional velocity components along x', y', z' direction respectively and u, v, w are the dimensionless velocity along x', y', z' direction respectively. p' is the modified pressure which includes gravitational and centrifugal force.
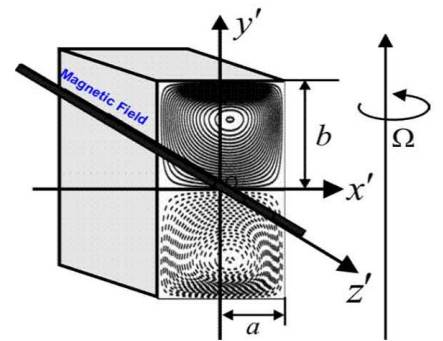
The assumption of fully developed flow means that except for the pressure derivatives z' are all set to zero. The dependent and independent variables are non dimension-lized as follows:

Figure 1: Co-ordinate system in a Rotating Straight Duct

$$u' = \frac{\upsilon}{a}u ; \quad x' = xa ; \quad p' = \frac{\upsilon^2}{a^2}\rho p ; \quad v' = \frac{\upsilon}{a}v ; \quad y' = y\,a ; \quad w' = \frac{\upsilon}{a}w ;$$
$$z' = 0,$$

where the variables with prime are dimensional quantities and $"a"$ be the half width of the cross section of the duct. Under the above assumption, the governing equations are;

$$u\frac{\partial u}{\partial x} + v\frac{\partial v}{\partial y} = -\frac{\partial p}{\partial x} + \left(\frac{\partial^2 u}{\partial x^2} + \frac{\partial^2 u}{\partial y^2}\right) - T_r w - M_g u \qquad (1)$$

$$u\frac{\partial v}{\partial x} + v\frac{\partial v}{\partial y} = -\frac{\partial p}{\partial y} + \left(\frac{\partial^2 v}{\partial x^2} + \frac{\partial^2 v}{\partial y^2}\right) - M_g v \qquad (2)$$

$$u\frac{\partial w}{\partial x} + v\frac{\partial w}{\partial y} = D_n + \left(\frac{\partial^2 w}{\partial x^2} + \frac{\partial^2 w}{\partial y^2}\right) + T_r u \qquad (3)$$

where, Taylor number $T_r = 2\left(\dfrac{a^2\Omega}{\upsilon}\right)$, Magnetic parameter , $M_g = \dfrac{\sigma'}{\mu_e}a^2 B_0^2 = \sigma'\mu_e a^2 H_0^2$

Dean number $D_n = \dfrac{Ga^3}{\rho \upsilon^2}$ and equation of continuity $\dfrac{\partial u}{\partial x} + \dfrac{\partial v}{\partial y} = 0$

The boundary condition is that the velocities are zero at $x = \pm 1$ and $y = \pm\left(\dfrac{b}{a}\right) = \pm\gamma$ (aspect ratio).

The new variable $\bar{y} = \left(\dfrac{y}{\gamma}\right)$ is introduced where γ is the aspect ratio, $\gamma = \left(\dfrac{b}{a}\right)$. $u = -\left(\dfrac{\partial \psi}{\partial y}\right)$ and $v = \left(\dfrac{\partial \psi}{\partial x}\right)$ which satisfies the continuity equation The basic equations (1)-(3) become for ψ and w as:

$$\frac{\partial^4 \psi}{\partial x^4} + \frac{2}{\gamma^2} \frac{\partial^4 \psi}{\partial \bar{y}^2 \partial x^2} + \frac{1}{\gamma^4} \frac{\partial^4 \psi}{\partial \bar{y}^4} = -\frac{1}{\gamma^3} \frac{\partial \psi}{\partial \bar{y}} \frac{\partial^3 \psi}{\partial \bar{y}^2 \partial x} - \frac{1}{\gamma} \frac{\partial \psi}{\partial \bar{y}} \frac{\partial^3 \psi}{\partial x^3} + \frac{1}{\gamma^3} \frac{\partial \psi}{\partial x} \frac{\partial^3 \psi}{\partial \bar{y}^3} + \frac{1}{\gamma} \frac{\partial \psi}{\partial x} \frac{\partial^3 \psi}{\partial x^2 \partial \bar{y}}$$

$$-\frac{1}{\gamma} \frac{\partial w}{\partial \bar{y}} T_r + \left(\frac{1}{\gamma^2} \frac{\partial^2 \psi}{\partial \bar{y}^2} + \frac{\partial^2 \psi}{\partial x^2}\right) M_g \tag{4}$$

$$\frac{\partial^2 w}{\partial x^2} + \frac{1}{\gamma^2} \frac{\partial^2 w}{\partial \bar{y}^2} = -\frac{1}{\gamma} \frac{\partial \psi}{\partial \bar{y}} \frac{\partial w}{\partial x} + \frac{1}{\gamma} \frac{\partial \psi}{\partial x} \frac{\partial \psi}{\partial \bar{y}} - D_n + \frac{1}{\gamma} \frac{\partial \psi}{\partial \bar{y}} T_r \tag{5}$$

The boundary conditions for ψ and w are given by

$$w(\pm 1, \bar{y}) = w(x, \pm 1) = \psi(\pm 1, \bar{y}) = 0$$

$$\left(\frac{\partial \psi}{\partial x}\right)(\pm 1, \bar{y}) = \psi(x, \pm 1) = \left(\frac{\partial \psi}{\partial \bar{y}}\right)(x, \pm 1) = 0$$

Flux through the Straight Duct

The dimensional total flux Q' through the duct is $Q' = \int\limits_{-b}^{b}\int\limits_{-a}^{a} w\, dx'\, dy' = \upsilon a Q$

where $Q = \int\limits_{-\gamma}^{\gamma}\int\limits_{-1}^{1} w\, dx\, d\bar{y}$ is the non- dimension flux.

3. Calculation Technique

The simulations are based on the Spectral method is used as a numerical technique to obtain the solution. It is necessary to discuss the method briefly. The basic ideas of the Spectral and collocation methods are given below. The expansion by polynomial functions is utilized to obtain steady or unsteady solution. The series of the Chebyshev polynomial is used in the x and $\bar{y}$ directions where, x and $\bar{y}$ are coordinate variables. Assuming the flow is symmetric along the axial direction.

The expansion function $\phi_n(x)$ and $\psi_n(x)$ are expressed as ;

$$\phi_n(x) = (1 - x^2) T_n(x) \tag{6}$$

$$\psi_n(x) = (1 - x^2)^2 T_n(x) \tag{7}$$

where, $T_n(x) = \cos(n \cos^{-1}(x))$ is the Chebyshev polynomial.

The functions $w(x, \bar{y})$ and $\psi(x, \bar{y})$ are expanded as;

$$w(x, \bar{y}) = \sum_{m=0}^{M} \sum_{n=0}^{N} w_{mn} \phi_m(x) \phi_n(\bar{y}) \qquad (8);\quad \psi(x, \bar{y}) = \sum_{m=0}^{M} \sum_{n=0}^{N} \psi_{mn} \psi_m(x) \psi_n(\bar{y}) \tag{9}$$

where, M and N are the truncation numbers in the x and $\bar{y}$ directions respectively. The collocation method (Gottlieb and

Orszag [5]) applied in x and $\bar{y}$ directions yields a set of nonlinear differential equations for w_{mn} and ψ_{mn}. The collocation points are taken as $(x_i, \bar{y}_j)$

$$x_i = \cos\left[\pi\left(1 - \frac{i}{M+2}\right)\right] \qquad (i = 1, 2, \ldots\ldots, M+1) \tag{10}$$

$$\bar{y}_j = \cos\left[\pi\left(1 - \frac{j}{N+2}\right)\right] \qquad (j = 1, 2, \ldots\ldots, N+1) \tag{11}$$

The details calculation technique and arc-length method for critical calculations are not shown for brevity.

4. Results and Discussion:

The steady solution has been obtained by the graphical representation of the total flux (Q) versus Taylor number (T_r) at Magnetic parameter $(M_g) = 5000$, corresponding Dean number $(D_n) = 500$, 1000, 1500 and 2000 respectively where the aspect ratio $\gamma = 3.0$. The steady solution curves have been drawn by the path continuation technique in the range $50 \leq T_r \leq 100000$. The graphical representation has shown in Figure 2 for the total flux (Q) versus Taylor number (T_r) in the range $50 \leq T_r \leq 32000$. For sufficient accuracy, $M = 10$ and $N = 30$ in the numerical calculations have been considered. The steady solution curves have been obtained for aspect ratio $(\gamma) = 3.0$ and $M_g = 5000$ in the range $50 \leq T_r \leq 32000$. These solution curves denoted by t_1, t_2, t_3 and t_4 at the Dean number $(D_n) = 500$, 1000, 1500 and 2000 respectively for graph of the total flux (Q) versus Taylor number (T_r). For brevity, plots of the flow pattern are not shown in actual format. The flow pattern of the secondary flow and contours plot of the axial flow at several Taylor numbers (T_r) on the solution curve for constant ψ and w are shown in Figures (3)-(6). We look the figures from the upstream. Therefore in these figures, the structures of the secondary flow and the axial flow can be understood. $T_r = (500, 2500, 5000, 6000, 9000, 16000)$ on t_1 curve (see Figure 3); $T_r = (500, 2500, 3000, 6000, 7500, 14300, 16000)$ on t_2 curve (see Figure 4); $T_r = (500, 1500, 3000, 4300, 9700, 16000)$ on t_3 curve (see Figure 5); $T_r = (500, 1500, 3000, 4300, 9700, 16000)$ on g_8 curve (see Figure 6) have been taken where the stream lines of the secondary flow (top) and the contour plots of the axial flow (bottom) in each row from left to right with the increment $\Delta\psi = 0.045, 0.075, 0.070, 0.10$ and $\Delta w = 6.0, 10.0, 10.0, 20.0$ at Dean number $(D_n) = 500$, 1000, 1500 and 2000 respectively.
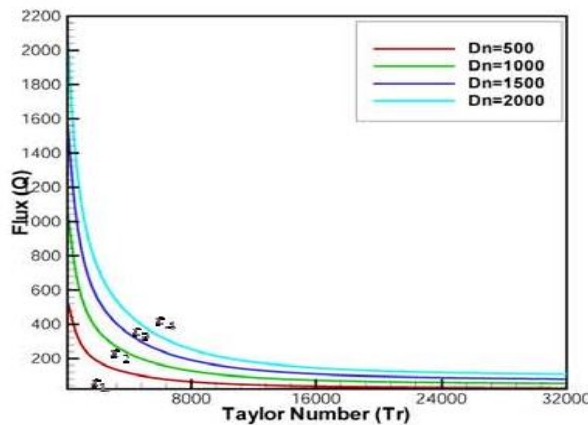

Figure 2: Steady solution for $M_g = 5000$, $D_n = 500$, 1000, 1500 and 2000, at $50 \leq T_r \leq 32000$

In Figures (3)-(6), the secondary flow, $(\psi \geq 0)$ in the upper region of the duct is the clock wise direction and counter clock wise in the lower part when $(\psi < 0)$. We have observed that the symmetric solution obtained in the range $50 \leq T_r \leq 32000$. The stream lines of the secondary flow are shown at various Taylor number (T_r) in the development of the vortex. 3-vortex,

4-vortex, 5-vortex and 6-vortex solution have been found in the secondary flow which is depend on the Taylor numbers (T_r) and Magnetic parameter (M_g). The contour plots of the axial flow has been formed the ring shape which are either single or double ring shape that appeared depends on the variation of Taylor number (T_r) as well as Magnetic parameter (M_g).
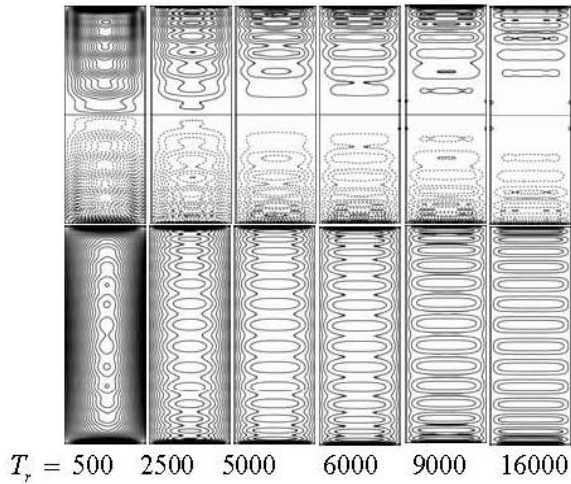

$T_r = 500 \quad 2500 \quad 5000 \quad 6000 \quad 9000 \quad 16000$
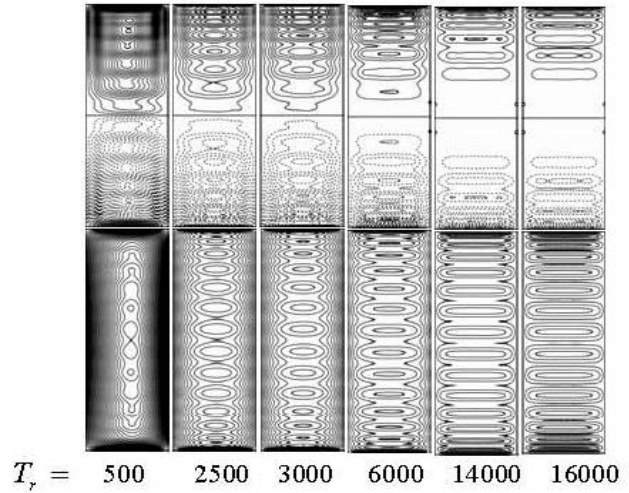
Figure 3: Stream lines of the Secondary Flow (top) and contours plot of Axial flow (bottom) in each row at Dean number $(D_n) = 500$ and $M_g = 5000$ for Flux (Q) versus Taylor number (T_r) at $T_r = 500$, 2500, 5000, 6500, 9000 and 16000.

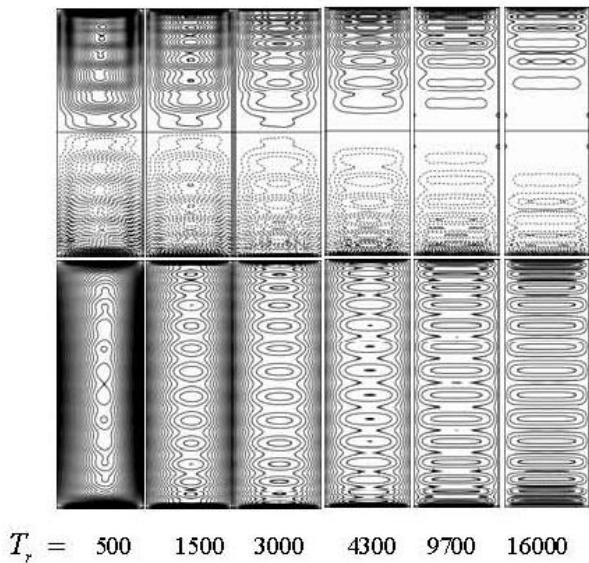$T_r = \quad 500 \quad 2500 \quad 3000 \quad 6000 \quad 14000 \quad 16000$

Figure 4: Stream lines of the Secondary Flow (top) and contours plot of Axial flow (bottom) in each row at Dean number $(D_n) = 1000$ and $M_g = 5000$ for Flux (Q) versus Taylor number (T_r) at $T_r = 500$, 2500, 3000, 6000, 14000 and 16000.

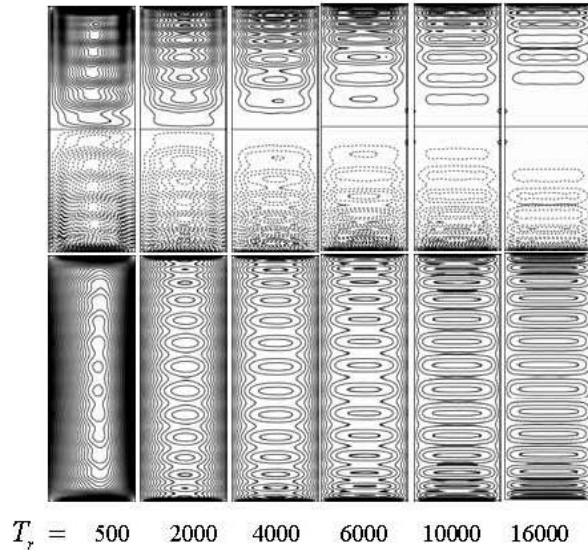$T_r = \quad 500 \quad 1500 \quad 3000 \quad 4300 \quad 9700 \quad 16000$

Figure 5: Stream lines of the Secondary Flow (top) and contours plot of Axial flow (bottom) in each row at Dean number $(D_n) = 1500$ and $M_g = 5000$ for Flux (Q) versus Taylor number (T_r) at $T_r = 500$, 1500, 3000, 4300, 9700 and 16000.

$T_r = \quad 500 \quad 2000 \quad 4000 \quad 6000 \quad 10000 \quad 16000$

Figure 6: Stream lines of the Secondary Flow (top) and contours plot of Axial flow (bottom) in each row at Dean number $(D_n) = 2000$ and $M_g = 5000$ for Flux (Q) versus Taylor number (T_r) at $T_r = 500$, 2000, 4000, 6000, 10000 and 16000.

5. Conclusion

According to the results, we have obtained the following important view:

1. For Magnetic parameter (M_g) and Taylor number (T_r) in both cases at high Dean number (D_n), steady solution has been obtained.

2. Anomalous vortices solution has been found for the maximum secondary flow pattern which depends on the Magnetic parameter (M_g) and Taylor number (T_r).

3. The symmetric flow structures at the maximum total flow region show almost the same flow behaviour in the range of $5 \leq M_g \leq 50000$. The strength of the secondary flows are decreases with the gradually increases of magnetic parameter (M_g).

4. Tendency of the axial flow structures to turn into the single, double and triple ring shape that appeared of course depends on the various Taylor number (T_r) at Dean number $(D_n) = 500$, 1000, 1500 and 2000 and Magnetic parameter (M_g).

6. Acknowledgements

7. References

[1] Alam *et al.* (2007) Flow through a rotating straight pipe with large aspect ratio, *Journal of Energy, Heat and Mass Transfer,vol 29,* 153-173.

[2] Barua, S.N (1955) Secondary flow in rotating straight pipe, *Proceeding of Royal Society of London A 227,* 133-139.

[3] Benton, G.S. and Baltimore, M.D. (1956) The effect of the earth's rotation on laminar flow in pipes, *Journal of Applied Mechanics, March Issue,* 123-127.

[4] Ito, and Nanbu, K. (1971) Flow in rotating straight pipes of circular cross-section, *ASME Journal of Basic Engineering, September issue,* 383-394.

[5] R. Moreau, S. Smolentsev and S. Cuevas(2010), MHD flow in an insulating rectangular duct under a non- uniform magnetic field, *PMC Physics B ,* 3, 2-43.

[6] V.Dousset(2009), Numerical simulations of MHD flows past obstacles in a duct under externally applied magnetic field, Ph.D. Dissertation, Coventry University

[7] Zengyu Xu, Chuanjie Pan, Wenhao Wei and Weishan Kang (2006) , Study of surface and bulk instabilities in MHD duct flow with imitation of insulator coating imperfections, *Fusion Engineering and Design* 81, 491–497

[8] Jalil, J.M. and Al-Taey, K.A. (2009), Natural convection in an enclosure under the influence of time- periodic magnetic field, *International Journal of Applied Electromagnetics and Mechanics, 31,* 97-111.

[9] L.H.Sheng (2012), Effects of Regional Magnetic Field on Rotating MHD flow Field of Unity Magnetic Prandtl Number, *Journal of Applied Mathematics,* Vol. 2012, ID 804105, 1-17.

[10] S. Chandrasekhar (1953), The stability of viscous flow between rotating cylinders in the presence of a magnetic field, *Proceedings of the Royal Society. London. Series A,* vol. 216, 293-309.

[11] Gottlieb, D. and Orszag, S. A. (1977) Numerical Analysis of Spectral Methods, *Society for Industrial and Applied Mathematics, Philadelphia.*